



1 **Synoptic- to meso-scale circulation connects fluvial and**
2 **coastal gravel conveyors and directional deposition of coastal**
3 **landforms in the Dead Sea basin**

4 Haggai Eyal^{1,2}, Moshe Armon^{1,3}, Yehouda Enzel¹, Nadav G. Lensky^{2,1}

5 ¹The Freddy & Nadin Herrmann Institute of Earth Sciences, The Hebrew University of Jerusalem, The Edmond
6 J. Safra Campus, Givat Ram, Jerusalem 91904, Israel

7 ²Geological Survey of Israel, 32 Yesha'yahu Leibowitz, Jerusalem 9371234, Israel

8 ³Institute for Atmospheric and Climate Science, ETH Zurich, 8092 Zürich, Switzerland

9 *Correspondence to:* Haggai Eyal (haggai.eyal@mail.huji.ac.il) and Nadav G. Lensky (nadavl@gsi.gov.il)

10

11 **Abstract.** Streams convey coarse-clastic sediments towards coasts, where interactions with deltaic and coastal
12 processes determine the resultant landscape morphology. Although extracting hydroclimatic signals from
13 landscapes is a desired goal, many studies rely on interpreting paleoclimatic proxies and the link between
14 depositional/geomorphic processes and the hydroclimate remains vague. This is a consequence of the challenge
15 to link processes that often are studied separately, span across large spatial and temporal scales including synoptic-
16 scale hydroclimatic forcing, stream flows, water body hydrodynamics, fluvial and coastal sediment transport, and
17 sedimentation. Here, we explore this chain of connected processes in the unique setting of the Dead Sea basin,
18 where present-day hydroclimatology is tied closely with geomorphic evolution and sediment transport of streams
19 and coasts that rapidly respond to lake-level fall. We use a five-years-long (2018-2022) rich dataset of (i) high-
20 resolution synoptic-scale circulation patterns, (ii) continuous wind-wave and rain-floods records, and (iii) storm-
21 scale fluvial and coastal sediment transport of varied-mass, ‘smart’ and marked boulders. We show that
22 Mediterranean cyclones approaching the eastern Mediterranean are the main circulation pattern that can provide
23 sufficient rainfall and winds that concurrently activate two perpendicular sediment conveyors: fluvial (floods) and
24 coastal (wind-waves). The synoptic-scale westerlies ($>10 \text{ m s}^{-1}$) are orographically funneled inside the Dead Sea
25 rift valley, turning into surface southerlies. They generate 10-30 high-amplitude northward propagating storm
26 waves per winter, with $<4 \text{ m}$ wave height. Such storms transport cobbles for hundreds of meters alongshore, north
27 of the supplying channel mouths. Towards the decay of the storm wave, the high-altitude synoptic westerlies
28 provide moisture to generate 4-9 flash-floods, delivering unsorted coarse gravels into the basin. These gravels are
29 dispersed alongshore by waves only during subsequent storms. As storm waves dominates and are $>$ five times
30 more frequent than flash-floods, coarse-clastic beach berms and fan-deltas are deposited preferentially north of
31 channel mouths. This depositional architecture, controlled by regional hydroclimate, is identified for both the
32 modern and Late Pleistocene coast and delta environments, implying that the dominance of present-day
33 Mediterranean cyclones has persisted in the region since the Late Pleistocene when Lake Lisan occupied the basin.



34 1. Introduction

35 Streams and coasts interact and convey coarse sediments. Streams deliver coarse-clastic sediments towards the
36 coast, where the interactions with coastal processes and sediment redistribution in the basin determine deltaic and
37 coastal geomorphology and sedimentology (Ashton et al., 2013; Galloway, 1975; Postma, 1995). While modern
38 deltas and coasts are desired areas for settlements, agriculture, and industry (e.g., Syvitski et al., 2009), ancient
39 deltaic and coastal successions are potential reservoirs of hydrocarbons and water (e.g., Elliot, 1986). Globally,
40 such reservoirs are formed also under receding water levels when the continental shelf and/or slope are exposed,
41 triggering evolution of streams in response to base level fall, and coarse sediment delivery from highstand to
42 lowstand deltas (e.g., Blum et al., 2013) (Fig. 1). Despite the importance of understanding common controls over
43 these jointly operating coarse-clastic conveyors, they are commonly studied separately.

44 Deltaic architecture is defined on the one hand, by the fluvial regime depending on the hinterland characteristics
45 of the watershed, where climate generates flows carrying sediment load into basins. On the other hand, sediment
46 redistribution and deposition are dictated by the shape, size, bathymetry of a basin, and by the hydrodynamics of
47 waves, currents, tides, and the rate of level changes of the water body occupying the basin (see Fig. 1 in Coleman
48 and Prior, 1982; Postma, 1990; Elliot, 1986). This wide range of influencing factors results in diverse types of
49 deltaic depositional configurations (Postma, 1990, 1995), from which it is challenging to decode hydroclimatic
50 and environmental signals, even in modern environments and more so from past sedimentary records (Hansford
51 and Plink-Björklund, 2020).

52 In modern *fluvial sediment conveyors*, atmospheric circulation patterns (CPs) and their association with rainfall
53 and floods are extensively studied for specific watersheds and regions (e.g., Bárdossy and Filiz, 2005; Steirou et
54 al., 2017; Merz et al., 2021; Kahana et al., 2002). However, linking the CPs with sediment transport is lacking. A
55 separate body of research deals with flows in channels, their resultant bedload sediment transport (e.g., Reid et
56 al., 1985; Wang et al., 2015; Lekach and Enzel, 2021), channel morphology (e.g., Montgomery and Buffington,
57 1997), and channel mouth deposition (e.g., Bridge, 1993; Wright, 1977; Coleman and Prior, 1982). In modern
58 *coastal conveyors*, along the shores of oceans or lakes, only a small number of studies have associated CPs with
59 wave climates (Pringle et al., 2014, 2015; Solari and Alonso, 2017; Graf et al., 2013), few of them also attributed
60 these processes to either longshore transport of sand (e.g., Goodwin et al., 2016), or shoreline erosion (Meadows
61 et al., 1997; Pringle and Stretch, 2021). This small body of research stems from the complex link between
62 synoptic-scale circulation, waves, and their resultant sediment transport; processes occurring over a wide range
63 of spatiotemporal scales (Pringle et al., 2015, 2014, 2021; Solari and Alonso, 2017). Therefore, our knowledge
64 regarding the joint fluvial and coastal environments is fragmented, i.e., full linking of the chain of
65 processes/environments, from the synoptic-scale circulation conditions that generate rainstorms-floods, to wind-
66 waves and to sediment transport and deposition in each of the sediment conveyors and their interactions, is
67 missing.

68 The modern Dead Sea (see regional setting in the next Sect.) is a unique environment providing a “natural
69 laboratory” to study these processes. It has several advantages: (i) The small to medium-scale watersheds (10^1 -
70 10^3 kms) surrounding the lake (e.g., Enzel et al., 2008; Zoccatelli et al., 2019) enable to deeply study the relative
71 impact of different CPs on water discharge (Enzel et al., 2003; Kahana et al., 2002; Dayan and Morin, 2006) and
72 sediment delivery to the basin (Armon et al., 2018; Ben Dor et al., 2018; Armon et al., 2019). (ii) Fluvial and
73 coastal geomorphic responses occur rapidly in response to lake-level fall, enabling a study of real-time

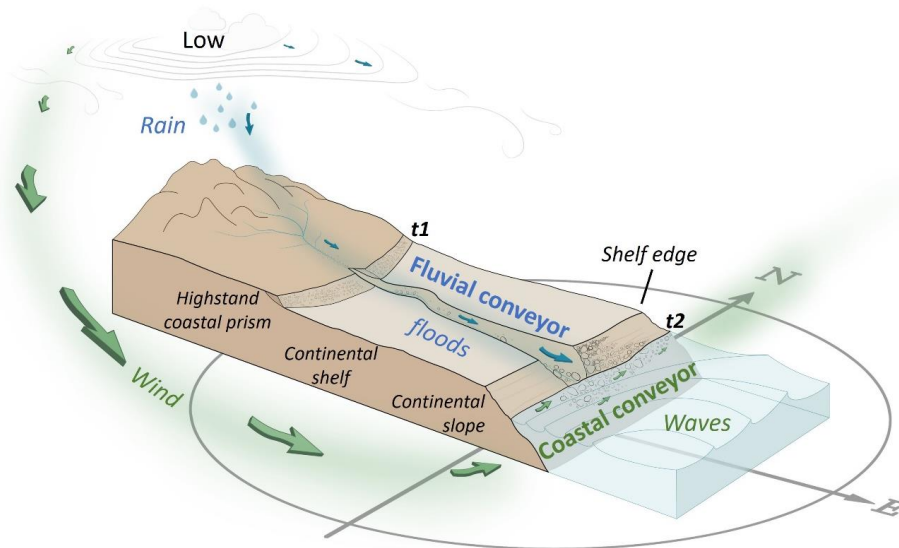


74 geomorphic processes and present-day sedimentary accumulation under forced regression and known
75 environmental forcing with implications to the sedimentary record (e.g., Bartov et al., 2006; Sirota et al., 2021).
76 (iii) Its sedimentary fill is accumulated and well-preserved in a terminal basin, thus it is extensively used to
77 reconstruct recent limnology and regional paleoclimatology-paleohydrology (e.g., Torfstein et al., 2015, 2013;
78 Huntington, 1911; Neugebauer et al., 2016; Kiro et al., 2017; Palchan et al., 2017; Ahlborn et al., 2018; Ben Dor
79 et al., 2018). Despite these advantages, interpretations are still mainly inferred based on selected specific proxies
80 and the geomorphic processes that led to deposition and their actual link to hydroclimate remains vague.

81 Armon et al., (2018) have linked the rain- and flood-generating CPs and the resulted sediment plumes dispersed
82 over the Dead Sea. Linking such sediment dispersion under the lake hydrodynamics is still missing, especially of
83 coarser sediments. Focusing on gravelly sediments, Eyal et al., (2019) established the recent evolution of an
84 incising stream transporting increasing volumes of gravelly sediment across the Dead Sea shelf. Then, from the
85 channel mouth, these coarse sediments are transported and sorted alongshore at the nearshore environment under
86 seasonal storm wave climates, forming well-sorted coastal landforms (Eyal et al., 2021). However, the
87 spatiotemporal interactions between the stream and coast and the linkage to or the control of the regional and
88 synoptic scale hydroclimatology needs elaboration to determine the chain of processes.

89 Therefore, we study here present-day climatic controls on coarse fluvial and coastal sediment transport by means
90 of rain, floods, wind, and waves data from the Dead Sea region. We explore the interactions between streams, the
91 coast and the actively forming coarse-clastic sedimentary record (Fig. 1). We search for the specific hydroclimatic
92 events controlling the formation of modern geomorphic/sedimentological record and potential insights when
93 interpreting similar past deposits. We use a five-years-long (2018-2022) dataset comprised of (i) high-resolution
94 synoptic-scale circulation conditions, (ii) continuous, wind-wave, and rain-floods records, and (iii) storm-scale
95 fluvial and coastal sediment transport measurements of ‘smart’ and marked boulders varying in mass. The
96 manuscript deals with the following questions:

- 97 (1) What is the nature of atmospheric CPs and hydrometeorological conditions activating these fluvial and
98 coastal conveyors?
- 99 (2) What are the hydroclimatic thresholds in terms of intensity-duration of the rain, and the magnitude of the
100 floods, winds and waves for transport and deposition of coarse gravel in this currently regressive lake?
- 101 (3) How do rain-producing floods and wind driven waves interact to generate a coastal geomorphic record
102 with a specific sedimentary architecture?
- 103 (4) What can we learn from the modern sedimentary environment formed by the two conveyors on past
104 geomorphic records?



105 Figure 1: Schematic illustration of the concepts of sediment transport via the stream and coast explored in this study. The
106 forcing/initiation is at the largest scale; low-pressure atmospheric circulation pattern activates both the fluvial sediment
107 conveyor by generating rainstorms and floods that transport coarse sediments into a receding basin (blue), and the coastal
108 sediment conveyor, in which wind-driven waves obliquely attack the beach and generate longshore sediment drift (green).
109 We discuss the dynamic case during water level lowering. t1 and t2 denote the position of highstand and lowstand
110 shorelines. In the case of the Dead Sea t1 represents the middle of the 20th century and t2 the 21st century.

111 2. The Dead Sea Regional settings

112 The Dead Sea basin is a narrow depression, 150 km long and 15–20 km wide, extending south-north (Fig. 2a)
113 along an actively subsiding tectonic basin of the Dead Sea transform (Garfunkel and Ben-Avraham, 1996). Since
114 the late Miocene, the basin is occupied by lacustrine water bodies, expanding and contracting due to climatically-
115 induced water balance and the physiography of the basin (e.g., Zak, 1967; Neev and Emery, 1967; Bartov et al.,
116 2002; Manspeizer, 1985). During wet and dry climates, the lake level rose and fell, and its area extended and
117 contracted, respectively (e.g., Bartov et al., 2003, 2006; Bookman et al., 2006; Enzel et al., 2003). The fluvial and
118 coastal geomorphic responses to these fluctuating lake levels have left well-preserved fan-deltas, paleo-shorelines,
119 and mudflats, related to the Late Pleistocene Lake Lisan (Bowman, 1971; Amit and Gerson, 1986; FROSTICK
120 and REID, 1989; Abu Ghazleh and Kempe, 2009) and the Holocene Dead Sea (Enzel et al., 2006., and chapters
121 in Enzel and Bar-Yosef, 2017) (Fig. 2a).

122 2.1 Geomorphic evolution of streams and coasts in response to shelf and slope exposure

123 The anthropogenically-induced level decline of the modern Dead Sea, at $>1 \text{ m y}^{-1}$ (Lensky et al., 2005), due to
124 water diversions, results in exposure of landscapes considered as fast-forming analogs to the eustatic emergence
125 of continental shelves and slopes (Dente et al., 2017, 2018; Eyal et al., 2019). The Dead Sea shelf and slope are
126 mainly comprised of clay silt, laminated, lacustrine deposits over which streams (e.g., Dente et al., 2017, 2018,



2021; Ben-Moshe et al., 2008; Bowman et al., 2010; Eyal et al., 2019) and coasts (e.g., Bowman et al., 2000; Bookman et al., 2006; Eyal et al., 2021; Enzel et al., 2022) rapidly evolve and can be studied at the field scale in real-time and at storm- to multi-year resolutions. In the north-western edge of the lake, at the lower reach of the well-studied ephemeral stream of Nahal (wadi) Og (Fig. 2b-d), hydrological connection with the fast-receding coastline is maintained by a cross-shelf incision and elongation. Channel bed steepens (channel slope >1.1%), narrows, and thus increased volumes and clast sizes of coarse sediment are transported to the receding shoreline intensify with time (Eyal et al., 2019). Gravels are comprised of carbonates and some chert and their intermediate axes length range between 0.05-0.4 m. From the tributary mouth, the unsorted fluvially-derived sediments are then transported northward and sorted along the shore, under winter storm waves (Figs. 1, 2d). This process was measured, quantified, and modelled at the individual storm scale, determining that the coastal longshore sorting is a direct manifestation of wave climate (Eyal et al., 2021). The interplay between fluvial sediment supply and longshore transport during winters and significant lake-level decline during summers, results in an annual separation between individual beach berms which practically, are fossilized, thus preserving their original coastal sorting (Eyal et al., 2021); i.e., there is no reactivation by subsequent storm waves of the coastal sediments, as occurs in most shores of earth.

142 2.2 Hydroclimate

143 2.2.1 The potential synoptic-scale climatic drivers at the eastern Mediterranean

144 Four major seasonal synoptic systems prevail in the eastern Mediterranean during wind and rain storms that affect
145 the Dead Sea region:

- 146 (i) In winter (mainly December-February), Mediterranean cyclones (MCs) (e.g., Alpert et al., 1990a), also
147 termed Syrian or Cyprus lows, depending on the respective location of their centers, dominate the stormy
148 weather (Alpert et al., 1990a; Alpert and Shay-El, 1994). These extratropical cyclones draw moisture
149 from the Mediterranean and convert it into moderate rainfall over broad areas (e.g., Ziv et al., 2015;
150 Kushnir et al., 2017). At the regional scale, during the passage of these storms, winds are generally
151 changing from easterlies into westerlies.
- 152 (ii) In autumn (October-December), Red Sea troughs (RSTs) are most common (e.g., Kahana et al., 2002),
153 while their “active” variant generates localized and intense rainfall with high spatial variability (Armon
154 et al., 2018, 2019, 2020; Dayan and Morin, 2006; Belachsen et al., 2017; de Vries et al., 2013; Tsvieli
155 and Zangvil, 2007). The non-active RST usually brings dry easterly winds at the surface (Saaroni et al.,
156 1998).
- 157 (iii) In spring (March-May), Sharav lows are frequent in the southeastern Mediterranean (Northern Egypt and
158 Israel), generating warm and dusty winds (e.g., Alpert and Ziv, 1989) with rarely occurring rains and
159 high velocity westerly winds following their passage over the area.
- 160 (iv) In summer (June-September), the Persian trough (PT) prevails; low pressure trough extending from the
161 Persian Gulf to the northeast, along with a subtropical high that borders it from the southwest (Alpert et
162 al., 1990b); rainfall is scarce as large-scale atmospheric subsidence dominates the region (Rodwell and
163 Hoskins, 1996; Goldreich, 2003; Kushnir et al., 2017; Tyrlis and Lelieveld, 2013; Lensky and Dayan,
164 2015), and winds are rather consistently flowing from the north-west (e.g., Tyrlis and Lelieveld, 2013;
165 Dayan et al., 2017).



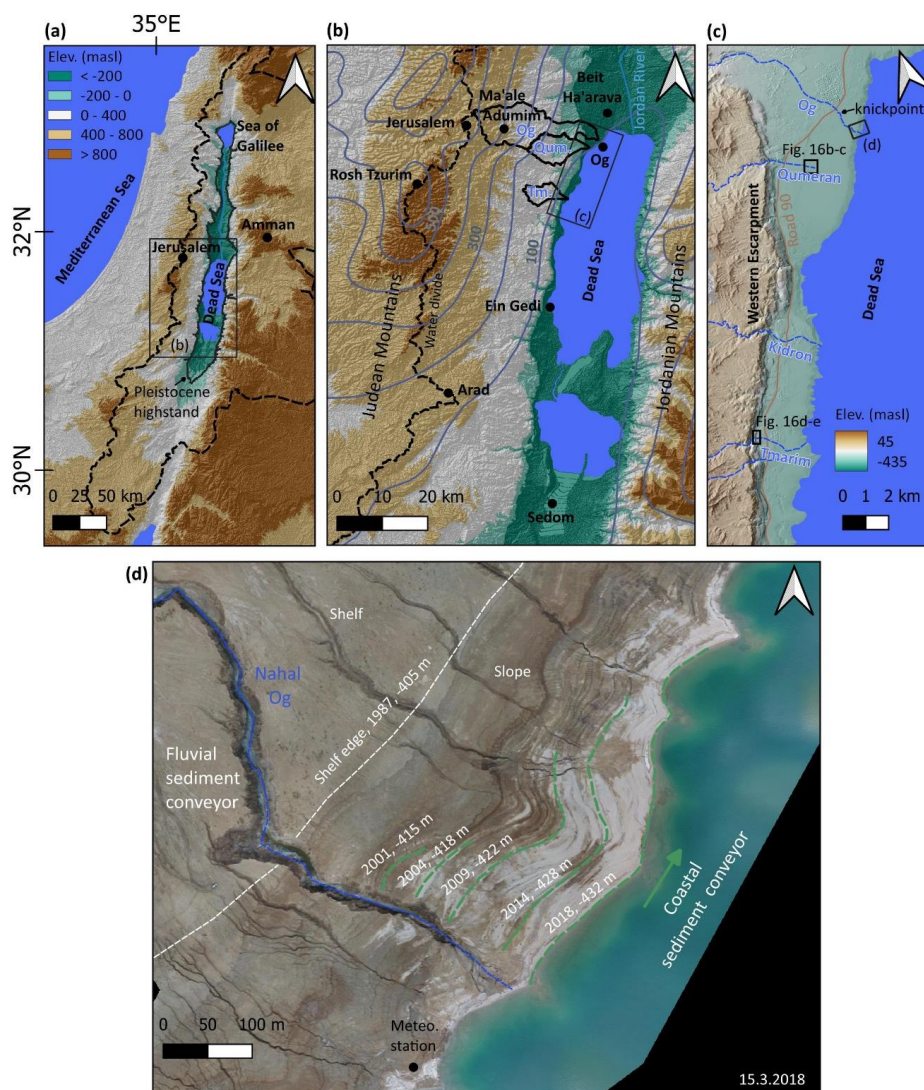
166 **2.2.2 The fluvial sediment conveyor**

167 Most of the precipitation that produces flash-floods in the Dead Sea region occurs in the heart of the winter, while
168 the full wet season lasts from October to May (Fig. 3a). Annually, the region experiences approximately 20 MCs
169 during winter and early spring with rainstorms typically lasting 2–3 days (Alpert et al., 2004a; Saaroni et al., 2010)
170 generating relatively high-volume floods (Enzel et al., 2003, 2008; Kushnir et al., 2017; Armon et al., 2018;
171 Shentsis et al., 2012). Smaller number of rainstorms during the autumn and spring are usually associated with
172 ARSTs (Armon et al., 2018).

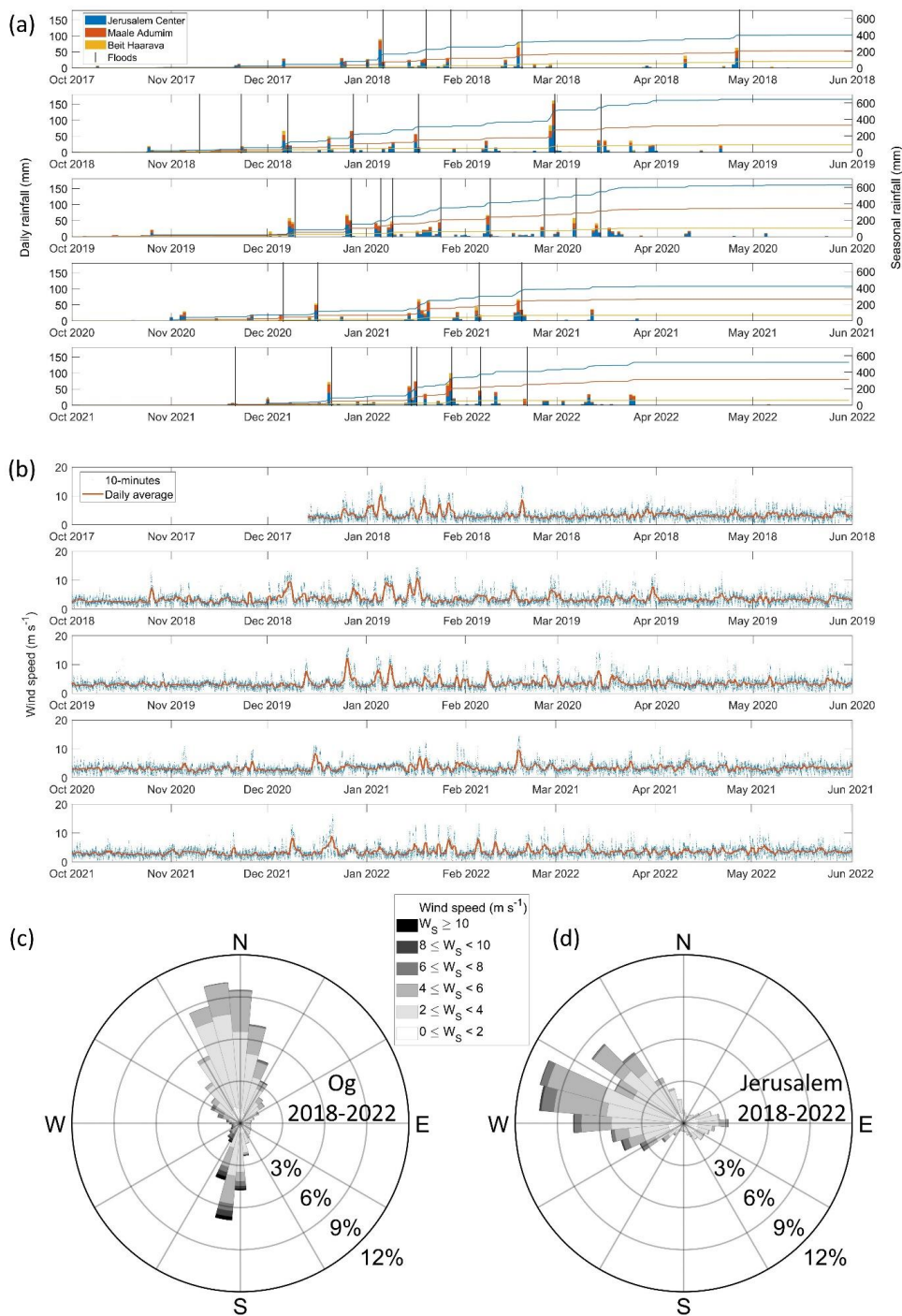
173 The western water divide of the larger Dead Sea tributaries is at the Judean Mountains with peaks up to ~1000
174 meters above sea level (masl) and Mediterranean/semi-arid climate (Fig. 2b). From the water divide eastwards,
175 the topography steeply slopes down to the Dead Sea at elevation of ~437 meters (in 2022) below sea level (mbsl)
176 over a short distance of ~30 km, resulting in a sharp climatic gradient (Fig. 3a) due to the orographic rain-shadow
177 effect (Goldreich, 2003; Kushnir et al., 2017). Thus, streams draining into the Dead Sea from the west are
178 ephemeral and are subjected to flash-floods during sufficient storm rainfall (e.g., Morin et al., 2009). For example,
179 in the Nahal Og watershed (137 km²), the climatic gradient ranges from >500 mm y⁻¹ in the western headwaters
180 to as low as ~50 mm y⁻¹ at the Dead Sea shore (Figs. 2b, 3a). The mean annual total rain volume falling over the
181 basin is ~40x10⁶ m³y⁻¹ (Haviv, 2007; Ben Moshe et al., 2008), of which only a small portion reaches the lake. The
182 highest peak discharge estimated for the stream by high-water marks after the rare flood of 2006, is 330 m³ s⁻¹
183 (Arbel et al., 2009). In Eyal et al., (2019), direct observations of flow marks at a specific location along the channel
184 were interpreted to represent the peak discharge of the common floods of ~20 m³ s⁻¹. Floods, lasting from a few
185 hours and up to a day, are generally short and quick response to high-intensity rain (e.g., Morin et al., 2009).

186 **2.2.3 The coastal sediment conveyor**

187 Winds along the Dead Sea have a bimodal directional distribution of either northerly or southerly direction (Fig.
188 3b,c) affected by the steep orography and north-south elongation of the Dead Sea rift (Bitan, 1974, 1976; Segal et
189 al., 1983; Vüllers et al., 2018; Kunin et al., 2019). During summer, the diurnal cycle dominates with dry and warm
190 northerly winds (<10 m s⁻¹) blowing stronger at night-time and weaker during the day, attributed to the meso-
191 scale circulation of the Mediterranean Sea breeze (Alpert et al., 1997; Gertman and Hecht, 2002; Lensky and
192 Dayan, 2012; Lensky et al., 2018; Hamdani et al., 2018; Kunin et al., 2019; Naor et al., 2017). During winter, the
193 diurnal cycle is less dominant as the above-mentioned synoptic scale circulation governs (Hamdani et al., 2018)
194 with southern windstorms, <20 m s⁻¹, lasting from a few hours to three days, blowing over the ~40 km south-to-
195 north lake fetch (Eyal et al., 2021). These high-magnitude winter windstorms generate waves with a maximum
196 height of ~4 m, wave periods of ~4 s, and wavelengths of ~25 m in the northeastern shores of the Dead Sea (Eyal
197 et al., 2021). During storms, waves approach the coast at ~45° (Eyal et al., 2021), forming optimum conditions
198 for unidirectional longshore drift (Longuet-Higgins, 1970; Van Hijum and Pilarczyk, 1982; Ashton and Giosan,
199 2011). Along the waterline of the Nahal Og coast, fluviially-derived gravels are distributed over a 20–30 m wide
200 strip, covering the lake floor by a monolayer, extending to a water depth of ~2.5 m; at this depth, a transition to
201 sandy-silty wave ripples is documented. The longshore transport and sorting of the coarse gravel and their link to
202 the wave climate were presented in Eyal et al., (2021) for three intensively-monitored storms.



203 Figure 2: Regional setting. (a) The eastern Mediterranean; shown are the Dead Sea watershed (black dashed line) and
 204 the highstand of the Late Pleistocene Lake Lisan, the predecessor of the Dead Sea (black line). (b) The Dead Sea region.
 205 Shown are the regional water divide of the Judean Mountains (dashed black line) and the watersheds of the studied
 206 tributaries: Og (Og), Qumeran (Qum.) and Tmarim (Tm.) (black polygons). Grey contours are isohyets (mean annual
 207 precipitation in mm y^{-1}). They present the rain shadow of the Judean Mountains towards the Dead Sea valley. Black
 208 dots are meteorological stations used in this study. (c) The tributaries draining into the north-western Dead Sea (blue
 209 dashed lines) and the Dead Sea western escarpment. (d) Aerial photograph of the lower reach of Nahal Og emphasizing
 210 the fluvial and coastal conveyors; note the increasing extension farther north, from the stream mouth, of the coastal
 211 gravel with lowering of the lake (green lines). It should be stressed that the tributaries north of Nahal Og drain the
 212 mudflat and do not carry gravel. Modified from Eyal et al., 2021.





214 **Figure 3: Rainfall and wind forcing during the five, intensively measured hydrological years: December 2017- June**
215 **2022. (a) Daily (bars, left-axis) and seasonal cumulative (lines; right-axis) rainfall measured, from west to east, in**
216 **Jerusalem (blue), Ma'ale Adumim (orange), and Beit-HaArava (yellow), representing the headwaters, the center, and**
217 **lower areas of the watershed, respectively (stations locations are presented in Fig. 2b). Vertical black lines are**
218 **occurrences of floods (Table S1 in the supplement). Note that most storms affect the entire region with consistent decline**
219 **in rainfall amounts away from the water divide. (b) 10-minutes (blue crosses) and daily average (orange line) wind**
220 **speed at Nahal Og mouth. Windrose for (c) Nahal Og (-430 masl) and (d) Jerusalem (835 masl) representing the**
221 **frequency and directionality of winds during the study period. Note the orthogonal wind directions; in the upper**
222 **watershed it is dominated by westerlies, while at the same time, within the Dead Sea rift valley, it is dominated by**
223 **northerlies and southerlies.**

224 3. Methods, data, and analysis

225 To unfold the chain of processes from the synoptic-scale climatology to rainstorms and flood hydrology and to
226 wind and wave climate, which are involved in the formation of the coastal sedimentary record along this regressive
227 lake, we assembled a high-resolution, rich dataset. It is comprised of: (1) Five-year long, continuous monitoring
228 of winds, waves, lake level, rain and flood hydrology. (2) Storm-scale sediment transport documented in the
229 channel and shore. (3) A combination of this dataset with atmospheric CPs using atmospheric reanalysis. These
230 observations constitute a one-of-a-kind dataset of coeval processes at such a resolution, undoubtedly for this
231 region and probably for elsewhere. Additionally, although these observations are based on only five years of data,
232 comparing the rainfall and wind timeseries with adjacent long record weather stations, indicates that these years
233 well represent the mean climatic conditions (Sect. S2 in the supplement).

234 3.1 Field measurements

235 *Wind* speed and direction at 10-min intervals were (a) measured at the Nahal Og mouth by a Gill-WindSonic
236 sensor located ~5 m above the lake surface, between December 2017 and June 2022, and (b) obtained from the
237 Israel Meteorological Service for the stations of Jerusalem Center (1999-2022), Ma'ale Adumim (2007-2022),
238 Ein Gedi (2007-2021), Rosh Tzurim (2001-2021), Arad (1999-2021), Sedom (1999-2021) and Beit Ha'arava
239 (2008-2022) (Fig. 2b).

240 *Waves* were measured at 4 Hz frequency by a water pressure sensor (Keller-PAA 36 Xi W) at water depth range
241 of 12 (December 2017) to 8 m (June 2022). Significant wave height and period were analyzed, accounting for the
242 attenuation of wave-induced pressure variation with water depth, and the temporal change of water depth due to
243 lake-level decline (Karimpour and Chen, 2017). From the continuous 4 Hz data, differences between maximum
244 and minimum pressure at 10-min resolution were normalized between 0 (no waves) and 1 (highest observed wave
245 height, $H = 4$ m) and used as proxies for the significant wave height (Fig. S3, Eyal et al., 2021). This was done as
246 the long time-series of 4 Hz measurements is incomplete. This analysis was validated by 16 Hz measurements of
247 RBR-solo-wave pressure sensor, deployed at 5-m water depth during three storm waves.

248 *Rain* data at 10-min intervals were obtained from the Israel Meteorological Service for the stations of Jerusalem
249 Center (1999-2022), Ma'ale Adumim (2008-2022) and Beit Ha'arava (2008-2022).

250 *A Flood Hydrology* data set was gathered from several sources (see Sect. S1 in the supplement), as no direct
251 discharge measurements exist in the watershed: (a) Observations obtained by Time-Lapse Cameras (TLCs) and



252 real-time field surveys, from which hydrographs were estimated using the manning formula (as in Eyal et al.,
253 2019) (when high flows occurred at night, high water marks were estimated from the daylight video). (b) Flood
254 reports obtained from the Israel Flash-flood Forecasting Center, Water Authority of Israel. (c) Flood reports
255 obtained from the Desert Floods Research Center categorized into no flood, weak flood, moderate flood, and large
256 flood. (d) Social network reports (e.g., Borga et al., 2019), providing an almost complete binary series of yes/no
257 flood occurrences and their estimated magnitude. These observations were synthesized to classify the floods into
258 four categories according to the estimated flood peak-discharge: low-flow floods, which due to transmission losses
259 do not reach the lake, weak floods, moderate floods, and large floods. Estimation of the extremity of the peak
260 discharge for each class was evaluated according to Rinat et al., 2021 (their Fig. 8). Cross-checking between the
261 information sources and close monitoring of the events during the measurement interval of 2017-2022 provides a
262 high level of certainty about the completeness of the flood time series. However, it must be noted that hydrograph
263 estimation gives rough values rather than exact high-resolution measurement data.

264 The *Dead Sea level* was obtained from Water Authority of Israel at a monthly resolution.

265 *Sediment transport* was measured using boulders with masses ranging between 0.5-100 kg. (a) Tens of boulders
266 were positioned in the upstream channel before a flood to estimate transport distances by a single event. (b) Along
267 the beach, using “smart” and painted boulders as described in Eyal et al., 2021, for three different storms.

268 *Late Pleistocene to modern fan-deltas* were analyzed by: (a) Airborne LiDAR-based DEMs for 2020, with
269 horizontal and vertical resolutions of 0.5 and 0.25 m pixel⁻¹, respectively (obtained from the Geological Survey
270 of Israel). (b) Orthophoto imagery and georeferenced aerial photographs from the years 1945, 1967, 1980, 1987
271 (obtained from the Survey of Israel). (c) A satellite image from 1971 (Corona mission, Grosse et al., 2005; data
272 available from <https://earthexplorer.usgs.gov>) with a spatial resolution of up to several meters per pixel. These
273 images were used to examine landscape change preceding the available LiDAR-based DEMs. They were also
274 used for mapping and determining the altitude of shorelines of the late 20th and 21st centuries, recognized on both
275 air photographs and LiDAR and of Late Pleistocene shorelines in Nahal Tmarim (location in Fig. 2b,c). DEM and
276 hill shade of 30 m pixel⁻¹ resolution obtained from Geological Survey of Israel were used for location maps (Figs.
277 2a,b, and 10a)

278 3.2 Data analysis

279 3.2.1 Storm detection

280 Over 120 storm waves were defined according to a physical threshold of the critical wave height for mobilization
281 of a 1 kg clast: $H_{cr} \approx 0.6$ m as determined previously by Eyal et al., 2021. A one-day interval was selected as
282 separating between individual storms. The timing of storm initiation and cessation was obtained using a lower
283 wave height threshold (e.g., Molina et al., 2019), $H \approx 0.15$ m, which is a sufficiently lower value to account for
284 the entire storm-wave duration (Fig. 4). As the waves are wind-driven (see below Sect. 4), windstorms were
285 defined according to the timing of the storm waves. This was done by applying the timing of the wave initiation
286 and cessation to the wind speed timeseries and redefining the windstorm initiation and cessation according to a
287 wind speed daily mean threshold of 3 m s⁻¹ (Fig. 4). This threshold optimally represents the storms following a
288 comparison with a range of thresholds (0.5 – 5 m s⁻¹). The storm peak is defined as the maximal wind value in the
289 interval between the initiation and cessation. Rainfall was analyzed at hourly intervals, accumulated from the 10
290 minutes data. Thirty-two flood-producing rainstorms were defined by detecting rainstorm peaks using a one-day



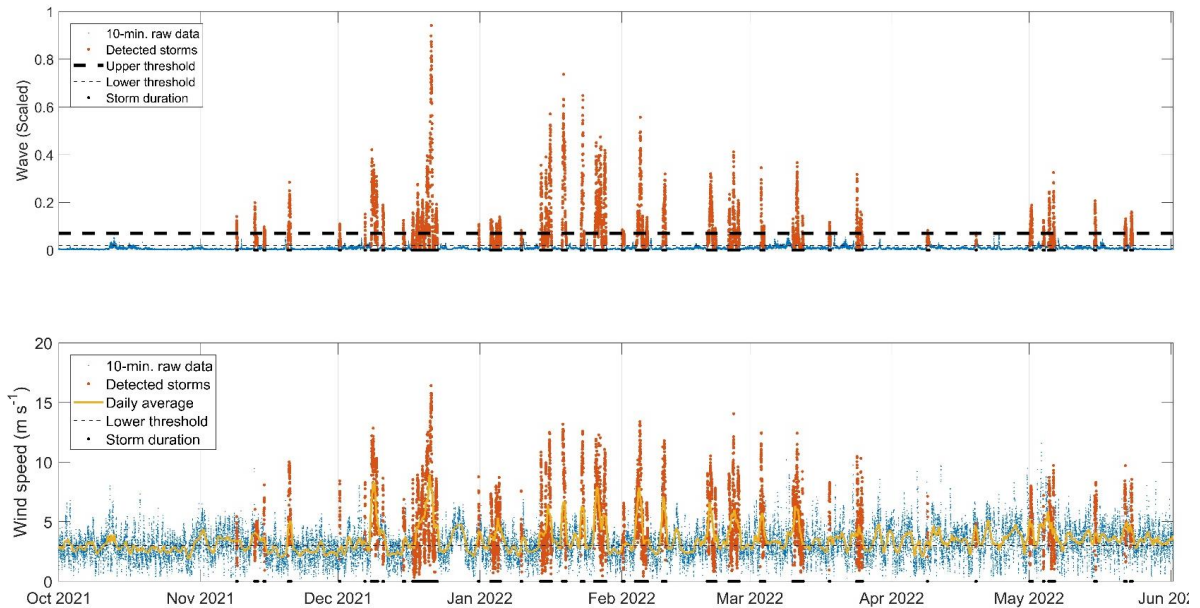
291 time interval before and after flood initiation. The timing of rainstorm initiation and cessation were redefined
292 using a 0.1 mm h^{-1} threshold and a separation of at least six hours between successive storms (e.g., Marra et al.,
293 2020).

294 3.2.2 Synoptic classification

295 We classified wind-waves-rain storms into four classes representing the most common synoptic circulation
296 patterns prevailing in the region (Sect. 2.2.1): Mediterranean Cyclones (MCs), Active Red Sea Troughs (ARSTs),
297 Persian Troughs (PTs), and Sharav Lows (SLs). To do so, we generalized the 19 classes obtained by the semi-
298 objective synoptic classification introduced by (Alpert et al., 2004b) for the eastern Mediterranean, which is based
299 on daily (12:00 UTC) meteorological fields at the 1000 hPa pressure level from the NCEP/NCAR reanalysis
300 (2.5° spatial resolution). We classified a storm as a MC if one of the storm days was considered as a MC. ARST
301 was defined if one of the storm days was considered as ARST with no MC prevalence. SL was classified if one
302 of the days during the storm was classified as SL, regardless of the other classes obtained by the semi-objective
303 classification. PT was classified only if it appeared in the summer months between June and September (e.g., Ziv
304 et al., 2004), even if it appeared with other classes. Otherwise, it was classified as a MC in accordance with weak
305 cyclones manifested as a shallow trough in the north-eastern Mediterranean (Ziv et al., 2022). The 13 cases
306 classified by the semi-objective classification as highs were manually inspected, and were reinterpreted as MCs,
307 as they represent the ending of MCs (e.g., Armon et al., 2019; Marra et al., 2021).

308 3.2.3 Composite and individual storm CPs

309 Composite and individual storm CPs were analyzed using data from the European Center of Medium-range
310 Weather Forecasts (ECMWF) Reanalysis model 5 (ERA5; Hersbach et al., 2020). Sea level pressure and 10-m
311 above ground wind maps were produced for the wind-wave storms at their onset, peak and cessation at a resolution
312 of 0.5° per pixel. Composite maps were obtained for (i) the mean conditions during the different storm parts both
313 for all CPs together and separately for, (ii) the lowest, intermediate, and highest terciles of the wave energy,
314 duration, and wave height, and (iii) the climatology of wave-producing CPs, non-wave-producing CPs, and the
315 anomaly of the wave-producing CP compared to the mean conditions of CP for the same period (2017-2022).



316

317 **Figure 4: An example of wind-wave storm detection during one hydrological year (2021-2022).** (a) Storm waves (orange
318 dots) were detected by an upper physical threshold following Eyal et al., 2021 (thick dashed black line), with the full
319 duration (black dots marked on the x-axis) defined by a lower threshold (thin dashed black line). (b) Windstorms
320 (orange dots) were defined according to the detected storm waves, with the full duration defined by a lower threshold
321 (dashed black line) following the daily average of the wind speed (yellow line).



322 4. The fluvial and coastal sediment conveyors and their synoptic-scale hydroclimatic control

323 We present insights from five representative storm-scale case studies in Sect. 4.1 for which we have detailed
324 measurements of sediment transport in the stream and coast under the forcing of atmospheric CPs, winds and
325 waves, rain, and floods (Figs. 5-9). Each component is described with respect to the timeline of a wind-wave
326 storm from its onset, rise, peak, decay, and cessation. Then, in Sect. 4.2, we present the separation of the wind
327 field into two levels with perpendicular directions, i.e., the regional surface wind during storms both outside and
328 inside the Dead Sea rift valley (Fig. 10). In Sect. 4.3 we generalize the processes leading to the activation of the
329 two sediment conveyors with a full analysis of the wind-wave storms and floods of the past five years with their
330 synoptic- and meso-scale climatology (Figs. 11-13). Given that MCs stand out as the main activators of the
331 sediment conveyors (Sect. 4.3 and Fig. 11), we describe the results according to the evolution of this synoptic-
332 scale CP and add information on other CPs when necessary.

333 4.1 The stream and coast at the storm scale

334 4.1.1 Storm-scale atmospheric CPs

335 At the onset of the wind-wave storms, the centers of the MCs are located north of the study region: (i) In the
336 vicinity of Greece, as far as ~1500 km northwest of the Dead Sea (Fig. 5c). (ii) In the eastern Mediterranean near
337 Cyprus, ~500 km northwest of the Dead Sea (Figs. 6-7c). (iii) In Syria or Iraq, 500-700 km north-northeast of the
338 Dead Sea (Fig. 8c). Only seldom storms occur when the cyclone is near the Dead Sea, in southern Israel (Fig. 9,
339 see a more detailed description of the event in Dayan et al., (2021) and in Rinat et al., (2021). The prevailing storm
340 circulation is of anti-clockwise westerly/south-westerly winds. Towards the storm peak, MCs focus (i.e., become
341 smaller), deepen, and move eastwards (Figs. 5-8d). In mature and ending stages of MCs, the regional westerly
342 flow and lowered inversion (Armon et al., 2019; Goldreich et al., 2004) are manifested by ‘mountain waves’; i.e.,
343 south-north elongated cloudy crests extending over the Jordanian mountains and plateau (Fig. 6h). The storm is
344 over when the low-pressure systems become larger, shallower, move further to the east, and a high-pressure
345 system invades the region (Figs. 5-8e).

346 4.1.2 Local wind and waves

347 While at the regional scale westerly flows dominates, at the local scale, over the Dead Sea itself, a sharp rise of
348 pronounced southern winds characterizes the onset of storms under MCs as measured along the Dead Sea shores
349 (Figs. 5-9b). With the intensification of the winds to $>10 \text{ m s}^{-1}$ and up to 20 m s^{-1} , northward-propagating waves
350 also intensify (Fig. 5-9b). At the end of the storm, diverse directionality that characterizes the pre- and post-storm
351 intervals of the wind (Figs. 5-9b) prevails, and the wind and waves quickly calm down.

352 4.1.3 Rain and floods

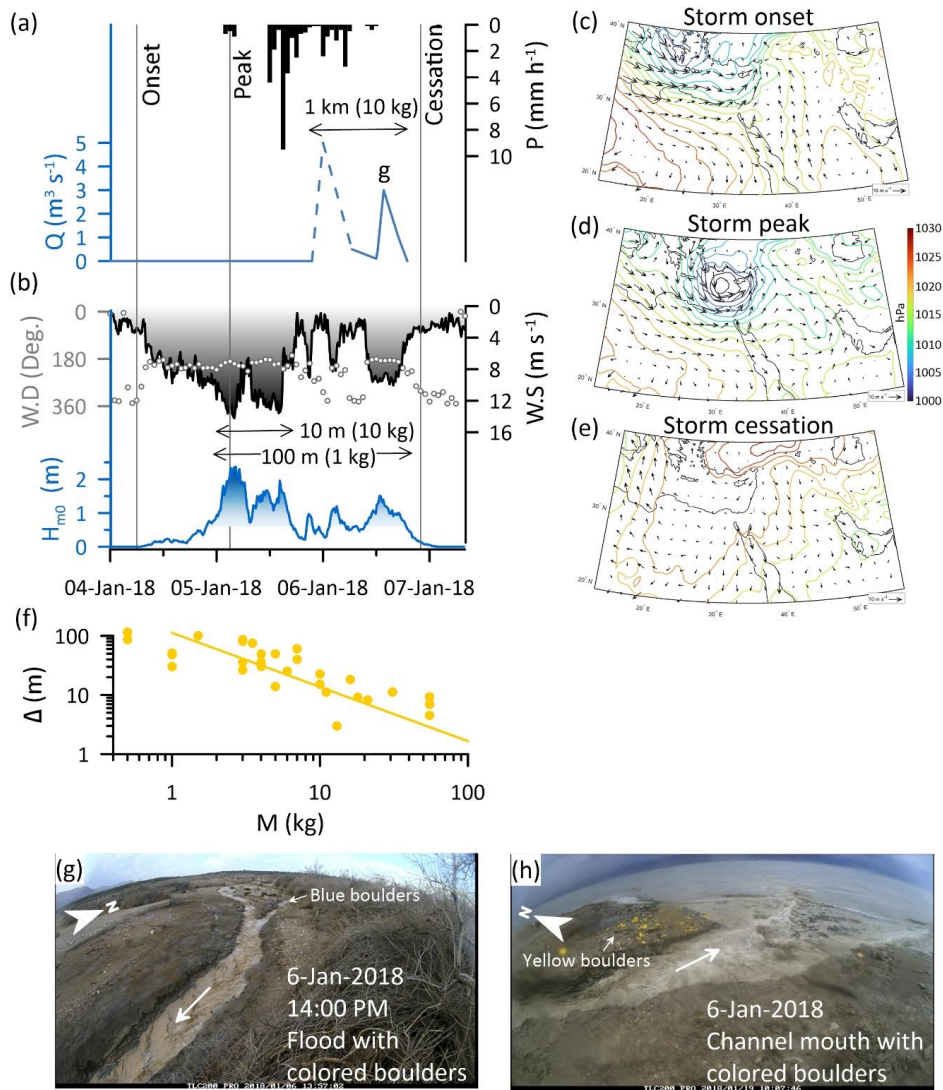
353 Rainfall in the drainage basin (Ma’ale Adumim) initiates coevally with the wind-wave storms, normally
354 intensifying after the storm wave peak (Figs. 5, 7–9a) or even during the peak (Fig. 6a), reaching moderate to high
355 intensities relative to this dry climate, of $> 5 \text{ mm h}^{-1}$ for the duration of at least an hour (Figs. 5–9a). Rainfall
356 intensity may comprise of several maxima, and accordingly, the flash-flood hydrograph presents several peaks
357 (Figs. 5, 7, 8a). Flood discharge ranges between weak floods ($\sim 5 \text{ m}^3\text{s}^{-1}$) (Fig. 5a), to the largest flood documented



358 between 2017-2022 with an estimated peak discharge of $120 \pm 30 \text{ m}^3 \text{ s}^{-1}$ (Fig. 8a). These floods typically last <24
359 h lagging a few hours after the rain peak; this important observation indicates that sediments are delivered to the
360 stream mouth towards the decay or end of the storm wave.

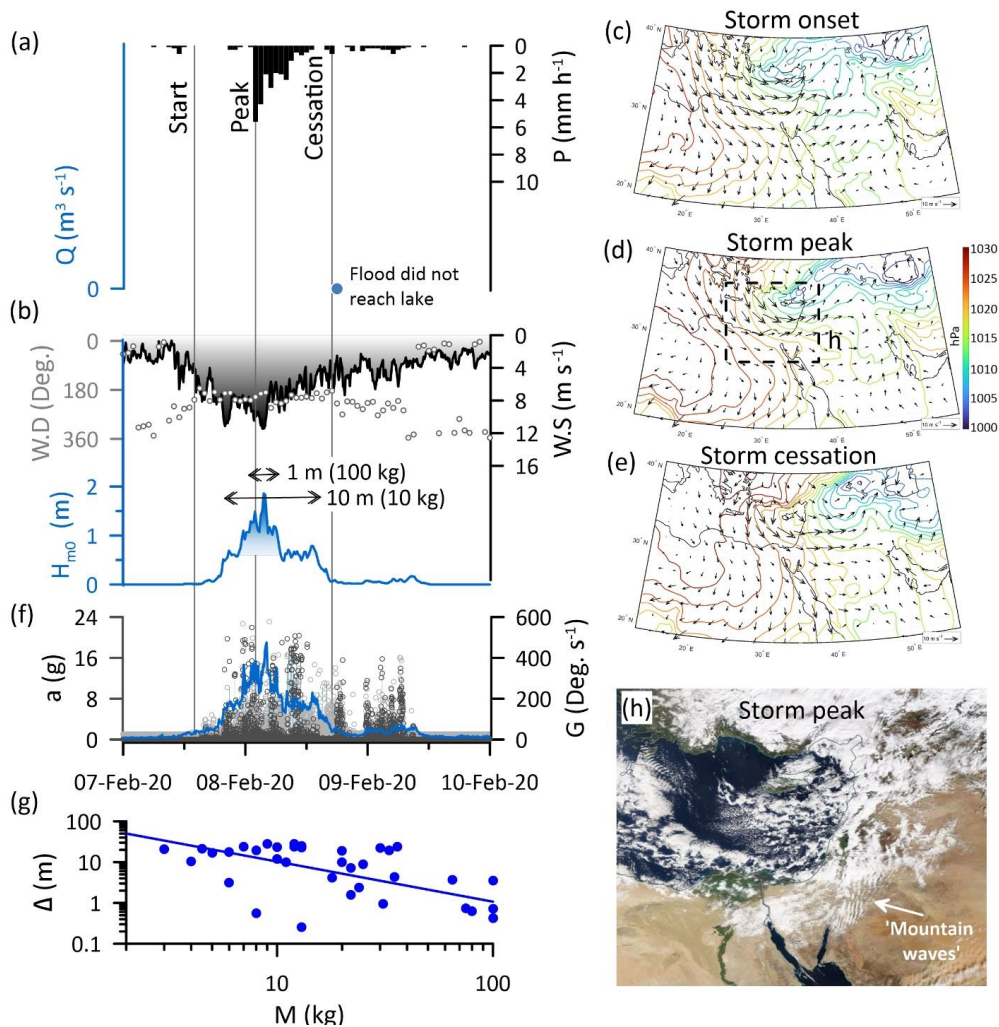
361 4.1.4 Sediment transport

362 With the rise of winds and waves and exceedance of the critical wave height (Fig. 4), certain clasts are mobilized
363 according to their mass as indicated by the recorded accelerations and rotations (Fig. 6f, Eyal et al., 2021). During
364 the storm peak, the highest accelerations and rotations are recorded (Fig. 6f). By the end of the storm wave, gravels
365 are sorted along the shore as the displacement decrease with increasing clast mass, according to a power law (Eyal
366 et al., 2021) (Figs. 5f, 6g, 9f). Larger clasts weighing ten of kilograms are transported to tens of meters, and finer
367 clasts weighing kilograms are transported hundreds of meters along the shore (Figs. 5f, 6g, 9f). Coevally, or by
368 the end of the storm waves, a flood reaches the stream outlet into the Dead Sea (Figs. 5–9a) transporting at a
369 single, relatively low-discharge flood, cobble-boulder sized clasts, >10 kg, along the incised channel across the
370 one-kilometer-wide shelf (Fig. 5a). The transport rate of boulders per single event along the shore is one to two
371 orders of magnitudes smaller relative to the transport in the stream. In the common case of floods that are generated
372 after the storm wave, delta deposition and sediment progradation of up to 20 m offshore is observed at the channel
373 mouth (Fig. 9g-i). In such a case, the activity of the coastal conveyor precedes the fluvial conveyor, and longshore
374 transport and sorting of the fluvio-deltaic sediments can only happen during the next storm. A different case is
375 when floods do not reach the lake and only the coast is activated by the storm, reworking the sediments delivered
376 by the previous storms in the season (Fig. 6a).

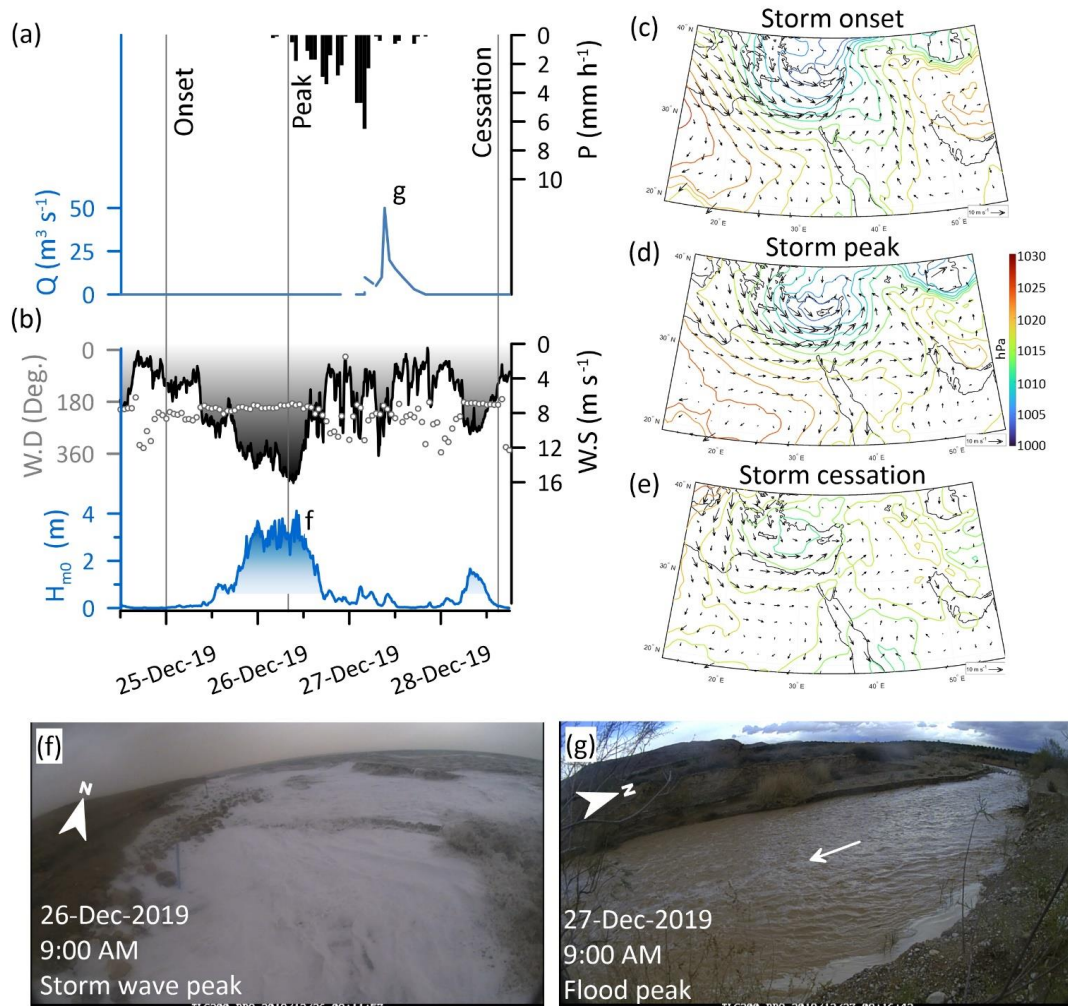


377

378 **Figure 5: Storm-scale observations (4-7 January, 2018) of the chain of processes from the synoptic scale atmospheric**
 379 **circulation that generate rainstorms-producing floods, wind-wave storms, resulting in fluvial and coastal sediment**
 380 **transport. (a) Hourly rainfall (P , Ma'ale Adumim, Fig. 2b), flood discharge (Q , solid line based on TLC and dashed**
 381 **line based on high-water marks). During this flood, colored cobbles-boulders were transported across the entire 1 km**
 382 **shelf width into the Dead Sea. (b) Wind ($W.S$ -wind speed, $W.D$ -wind direction in dots) and wave height (H -significant**
 383 **wave height, colored gradient fill indicates waves above transport threshold). (c, d, and e) CP maps of a deep**
 384 **Mediterranean Cyclone plotted according to the onset, peak, and cessation of wind, respectively. (f) Longshore**
 385 **displacement (Δ) of various-mass boulders (M) (yellow dots), transported from the channel mouth northward and**
 386 **sorted alongshore according to a power-law (yellow line), following Eyal et al., 2021. (g) The flood at the stream**
 387 **knickpoint where boulders were colored. (h) The flood flows into the Dead Sea, where coastal boulders are colored.**
 388

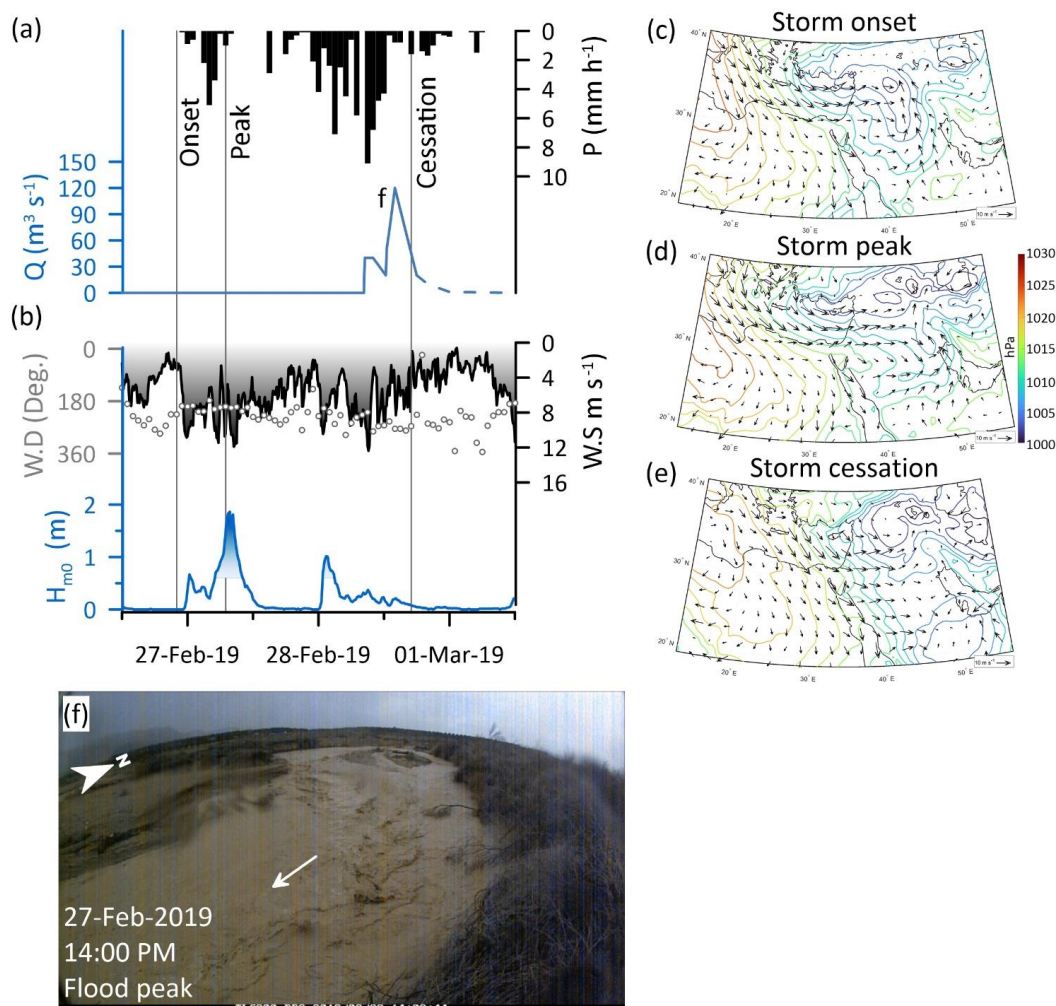


389 Figure 6: Storm-scale observations (7-9 February, 2020) of the chain of processes from the synoptic-scale atmospheric
 390 circulation that generate rainstorms-producing floods, wind-wave storms, resulting in fluvial and coastal sediment
 391 transport. (a) Hourly rainfall (P , Ma'ale Adumim, Fig. 2b), flood was generated but did not reach the lake. The timing
 392 of a first wave is marked by a blue dot. (b) Wind ($W.S$ -wind speed, $W.D$ -wind direction in dots), and wave height (H -
 393 significant wave height, colored gradient fill indicates waves above transport threshold). (c, d, and e) CP maps of a
 394 Mediterranean Cyclone plotted according to the onset, peak, and cessation of wind, respectively. (f) Resultant
 395 acceleration (a , grey dots) and rotations (G , black dots) recorded by five, various-mass smart boulders indicating the
 396 real-time motions of clasts under storm waves, following Eyal et al., 2021. (g) Longshore displacement (Δ) of various-
 397 mass boulders (M) (blue dots), transported from the channel mouth northward and sorted alongshore according to a
 398 power-law (blue line). (h) Aerial photograph of the eastern Mediterranean during the storm peak (8 February, 2020)
 399 obtained from <https://worldview.earthdata.nasa.gov/>, location in (d). Note the south-north elongated cloudy crests
 400 termed 'mountain waves', indicating on the synoptic westerly air flow.

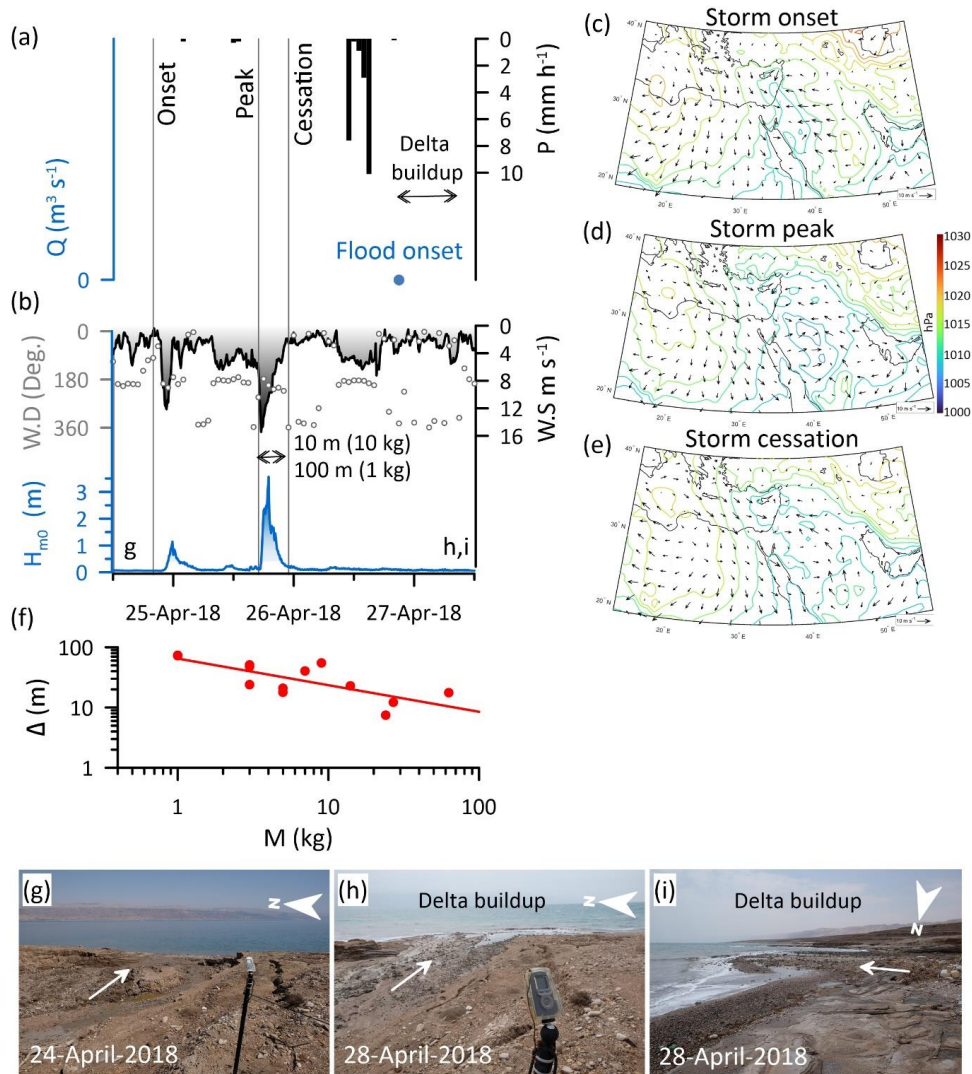


401

402 **Figure 7: Storm-scale observations (25-28 December, 2019) of the chain of processes from the synoptic-scale**
 403 **atmospheric circulation that generate rainstorms-producing floods, wind-wave storms, resulting in fluvial and coastal**
 404 **sediment transport. (a) Hourly rainfall (P, Ma'ale Adumim, Fig. 2b), flood discharge (Q, solid line-TLC). Wind (W.S-**
 405 **wind speed, W.D-wind direction in dots) and wave height (H-significant wave height, colored gradient fill indicates**
 406 **waves above transport threshold). This storm wave was the largest documented in our record (Video supplement). (c,**
 407 **d, and e) CP maps of a deep Mediterranean Cyclone plotted according to the onset, peak, and cessation of wind,**
 408 **respectively. (f) The storm wave during its peak, which is the highest in our record. (g) The flood peak downstream to**
 409 **road 90 (location in Fig. 2c).**



410 Figure 8: Storm-scale observations (27-28, February 2019) of the chain of processes from the synoptic scale atmospheric
 411 circulation that generate rainstorms-producing floods, wind-wave storms, resulting in fluvial and coastal sediment
 412 transport. (a) Hourly rainfall (P, Ma'ale Adumim, Fig. 2b), flood discharge (Q, solid line-TLC). This flood was the
 413 largest documented in our record (Video supplement). (b) Wind (W.S-wind speed, W.D-wind direction in dots) and
 414 wave height (H-significant wave height, colored gradient fill indicates waves above transport threshold). (c, d, and e)
 415 CP maps of a Mediterranean Cyclone centered to the east of the Mediterranean, with an extended trough to the eastern
 416 Mediterranean, plotted according to the onset, peak, and cessation of wind, respectively. (f) The flood peak downstream
 417 of Highway 90 (location in Fig. 2c).

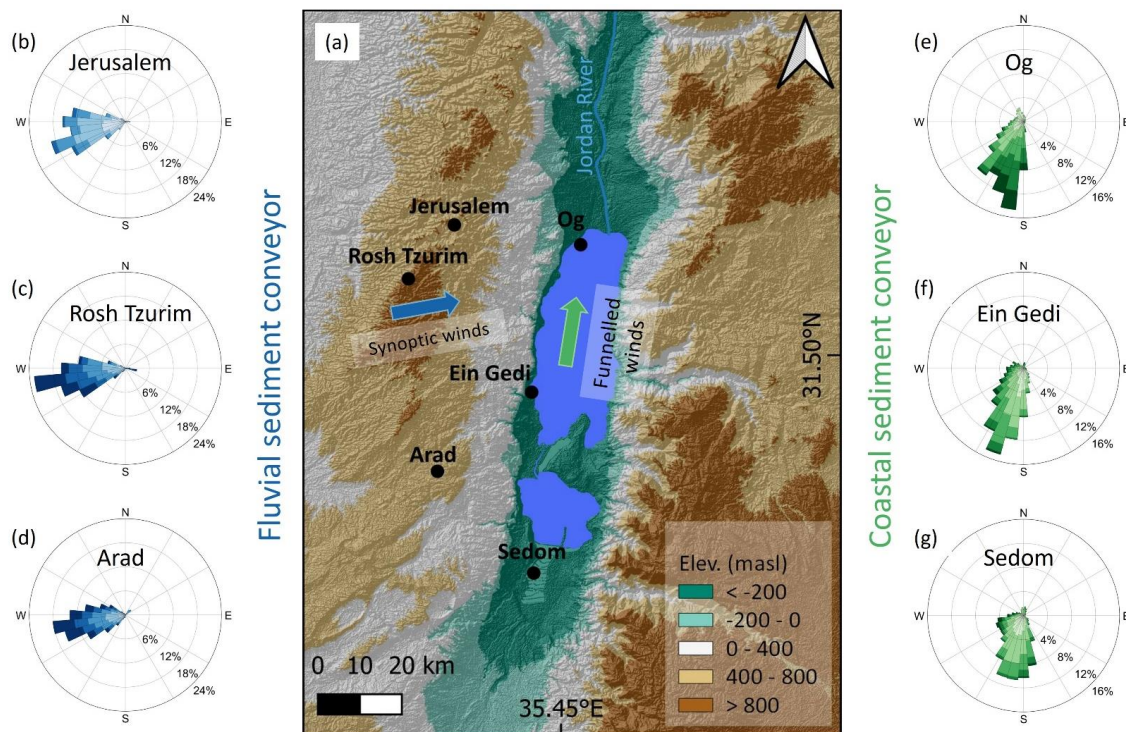


418 Figure 9: Storm-scale observations (25-27 April, 2018) of the chain of processes from the synoptic-scale atmospheric
 419 circulation that generate rainstorms-producing floods, wind-wave storms, resulting in fluvial and coastal sediment
 420 transport. (a) Hourly rainfall (P , Ma'ale Adumim, Fig. 2b). The flood discharge was high, as indicated from a field visit
 421 during this storm. (b) Wind (W.S.-wind speed, W.D.-wind direction in dots) and wave height (H -significant wave height,
 422 colored gradient fill indicates waves above transport threshold). (c, d, and e) CP maps of a southern-centered
 423 Mediterranean Cyclone plotted according to the onset, peak, and cessation of wind, respectively. This storm also was
 424 discussed in detail in Rinat et al., (2021) and Dayan et al., (2021). (f) Longshore displacement (Δ) of various-mass
 425 boulders (M) (red dots), transported from the channel mouth northward and sorted alongshore according to a power-
 426 law (red line), following Eyal et al., 2021. (g) The channel mouth before the storm. (h and i) The channel mouth after
 427 the flood ends with prominent fan-delta progradation of ~ 20 m offshore.



428 **4.2 Synoptic-scale and orographically channelled surface winds activating the two perpendicular sediment**
429 **conveyors**

430 During MC storms, synoptic-scale westerly circulation is consistent with measurements of surface wind in ground
431 stations, located along a south-north transect of the 600-1000 masl water divide at the Judean Mountains (Fig.
432 10a-d). Coevally, a transect of the winds within the Dead Sea rift valley at an elevation of ~400 mbsl, ~30 km east
433 of and sub-parallel to the water divide, indicates that the high-magnitude surface winds have a clear southern
434 directionality (Fig. 10a, e-g). We attribute this directionality change, from the regional westerlies into in-rift valley
435 southerlies during the same individual storm, to the orography-funneling effect of the Dead Sea valley with its
436 south-to-north oriented rift shoulders (e.g., Bitan, 1976). Consequently, we recognize that the winds associated
437 with the main synoptic-scale circulation pattern (MC) splits into two perpendicular directions; these two
438 hydroclimatic generators activate differently the coarse-sediment conveyors (Figs. 1, 10, Video supplement): (i)
439 Westerlies at high altitudes convey moisture from the Mediterranean Sea, with rainfall amounts tending to increase
440 when air parcels encounter the orographic barrier of the Judean Mountains and then decrease in the rain shadow
441 area of the Dead Sea rift valley (Sharon and Kutiel, 1986; Goldreich, 1994; Marra et al., 2022). This orographic
442 effect is an important permanent feature over the last millions of years since the rift reached its shape. This
443 orography determines the amount and distribution of rainfall over the western Dead Sea watersheds and, in turn,
444 the characteristics of floods, and with them the timing of sediment delivery into the basin. The conveyance of
445 moisture continues to the east of the Dead Sea and rainfall amount increases again with the upslope flow over the
446 Jordanian mountains >1000 masl (e.g., Armon et al., 2019); as a result, floods are generated, and sediments are
447 delivered to the Dead Sea from the eastern watersheds at the very end of the storms. (ii) At the surface, southerlies
448 blow perpendicular to and coeval with the synoptic-scale mountainous winds. The meso-scale funneling of winds
449 blowing over the lake results in south-to-north waves propagation and thus, at the coast, the redistribution of
450 sediments preferentially northwards from the channel mouths along the Dead Sea shores.
451 Weaker CPs have different air trajectories, but as long as the synoptic winds have a slight southern component,
452 the topography and shape of the Dead Sea rift margins govern, resulting in southerly-funneled winds. For example,
453 under ARST conditions, the synoptic scale wind is southeasterly, while the actual surface wind measurements are
454 pure southerlies (Fig. S4).



455

456

457 **Figure 10: Synoptic and meso-scale windstorms.** (a) Location map showing the two perpendicular directions of the
 458 winds flow during MC storms. (b, c, and d) Wind roses from three Judean Mountains water divide stations (locations
 459 are indicated in the map). These data show the western-southwestern high-magnitude winds during winter storms
 460 conveying at high altitudes the moisture for flood generation in the fluvial sediment conveyor (blue coloring). (e, f, and
 461 g) Wind roses from inside the Dead Sea rift valley. These data show the change in wind direction as the synoptic scale
 462 winds are funnelled in the rift and transformed into high-magnitude southerlies that generate the northward
 463 propagating storm waves activating the coastal sediment conveyor (green coloring). Legend of the wind roses appear
 464 in Fig. 3c-d.



465 **4.3 The sediment conveyors at the seasonal scale under a joint atmospheric circulation generator**

466 **4.3.1 The coastal conveyor at the seasonal scale**

467 Like the stream, the coast is activated mainly between December and March (Fig. 11) under MCs located north
468 of the Dead Sea region (Fig. 12). Each of the 128 classified storm waves (i.e., 10–30 storms per winter) are wind
469 driven and are correlated with high magnitude southern winds (Fig. S6). The wind and wave storm durations are
470 very similar or equal (Fig. 12a), ranging between several hours to three days, <1.5 days for the 25-75 percentiles
471 of the wind (Fig. 13a-b). The prevailing CP during 80% of the identified storms is MC (Fig. 12a), also causing
472 the highest storm wave energy with the longest duration of up to 3.5 days (Fig. S5). At the onset of storms, on
473 average, a deep low-pressure system, ~10 hPa below mean, is located in the vicinity of either Cyprus or Syria,
474 exhibited in the composite analysis as bi-center lows in these two regions, and the regional wind direction is
475 western, with a slight southern component over southern Israel (Fig. 13d). At storm waves peak, the low-pressure
476 system contracts its area and moves eastwards (Fig. 13e). Along the Dead Sea, the median wind speed at the
477 storms peak is of 10 m s^{-1} with short-term winds of up to $<20 \text{ m s}^{-1}$ and a clear southern direction. The wind-
478 driven northwards propagating waves, typically lagging the regional wind peaks by 0.5-2 h. Median wave height
479 is about ~1 m with maximal height of ~4 m. The cessation of storms is associated with significant shallowing of
480 the MC, appearance of high-pressure system and its advancement from the west, and a change of the mean wind
481 direction into northwesterly winds (Fig. 13f), funneled inside the Dead Sea valley into northerlies.

482 The non-MC storm waves are generated by low wave-energy CPs, mainly by Active Red Sea Troughs, (15% of
483 storm-waves producing CPs). The other 5% are caused by Persian Troughs and Sharav Lows, generating storms
484 lasting <10 h (Fig. 12a, Fig. S4). Practically, these storms have a minor impact on the coastal geomorphology and
485 sediment transport as the thresholds for the motion of clasts in the coastal conveyor are barely exceeded.

486 The comparison of the mean climatology of wind-wave producing MCs with the nonproducing MCs, show that
487 wind-wave producing MCs: (i) are characterized by stronger regional westerlies, and (ii) have ~3 hPa deeper low
488 center and an adjacent high of ~5 hPa higher located over Egypt and Turkey. This difference of ~8 hPa results in
489 steeper pressure gradients from the north and south of the MC and the generation of stronger winds (Fig. 14),
490 which are then funneled into southerlies at the local scale (Fig. 10).

491 **4.3.2 The fluvial conveyor at the seasonal scale**

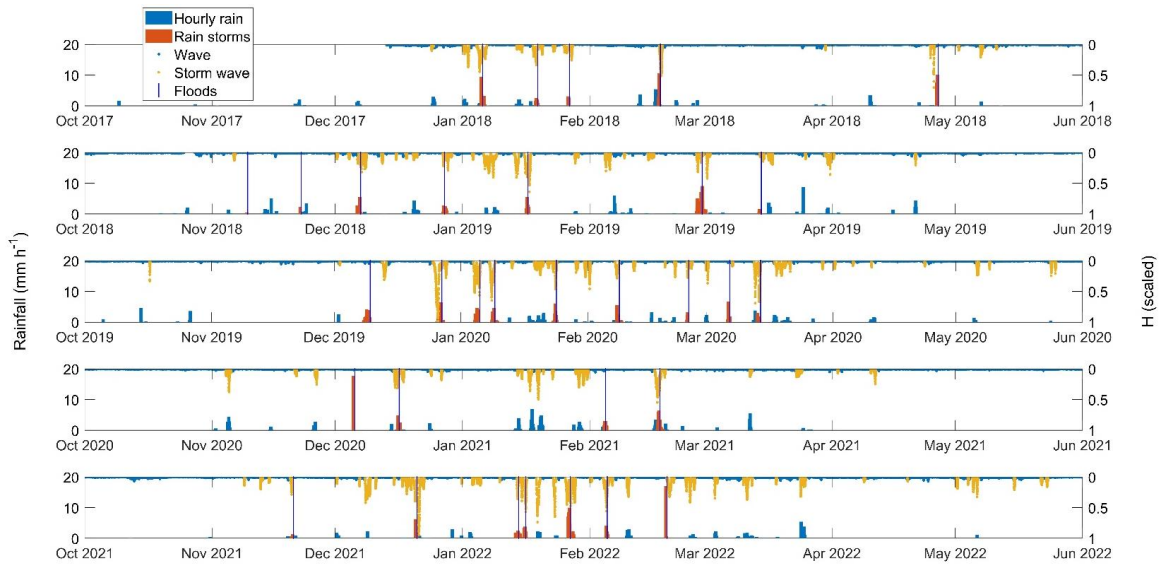
492 Flood-producing rainstorms in the stream occurred 4-9 times per season. Each of these rainstorms lasted between
493 a few hours and up to two days (Figs. 11, 12b) with a typical duration of 10-15 hours for the 25-75 percentiles
494 (Fig. 13c). These rainstorms have a median peak intensity of 5 mm h^{-1} for the duration of an hour (Fig. 13c), and
495 maximal intensities $<20 \text{ mm h}^{-1}$ (Fig. 11). Rain depth $>10 \text{ mm}$ per storm generates moderate or larger floods as
496 measured in the center of the Og watershed (Fig. S7). L 60% of the floods present low discharge with a peak
497 discharge $<10 \text{ m}^3\text{s}^{-1}$ or attenuate to such low flows that the floods do not reach the lake. Moderate floods (9 floods,
498 28%) experience peak discharge of $10\text{--}60 \text{ m}^3\text{s}^{-1}$ and the high-discharge floods (4 floods, 12%) have an estimated
499 peak discharge of $60\text{--}170 \text{ m}^3\text{s}^{-1}$. Under rare conditions extreme floods with a peak discharge $>170 \text{ m}^3\text{s}^{-1}$ can be
500 generated. For example, in 2006, an exceptional discharge of $330 \text{ m}^3\text{s}^{-1}$ (Arbel et al., 2009), equivalent to an



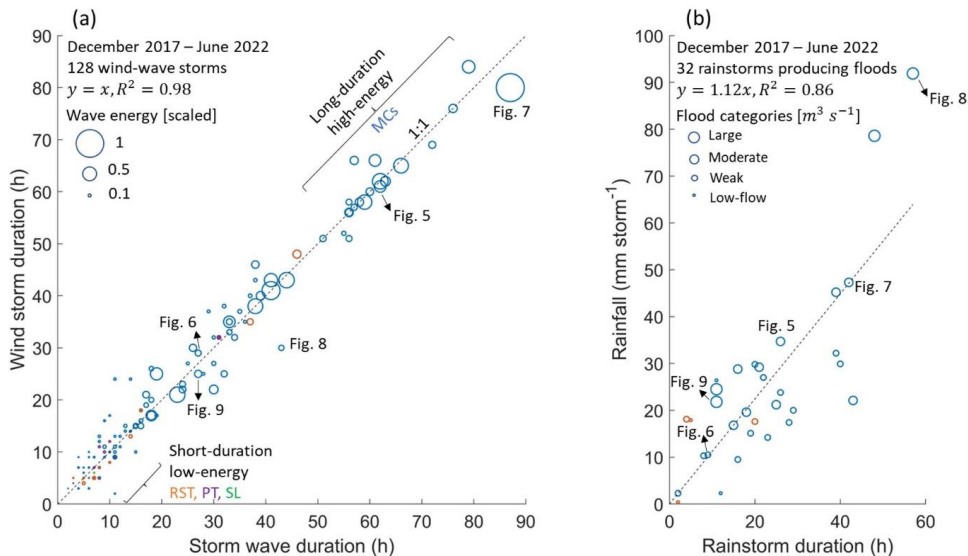
501 instantaneous rainfall intensity of 8.7 mm h^{-1} over the entire watershed, has been indirectly estimated in Nahal Og
502 based on high-water marks.

503 Approximately 85% of the flood-producing rainstorms were generated by MCs, with all the moderate to large
504 floods generated by this CP type. Moreover, these rainstorms occurred coevally with storm waves occurring under
505 the same MCs (Fig. 11). For MCs, rainfall amounts increase with storm duration (Fig. 12b), a relation that we
506 attribute to the characteristically continuous, wide coverage of rainfall during MCs (Armon et al., 2018). The
507 finding is coherent with similar analysis that was applied for the adjacent and larger Lower Jordan River (Armon
508 et al., 2019).

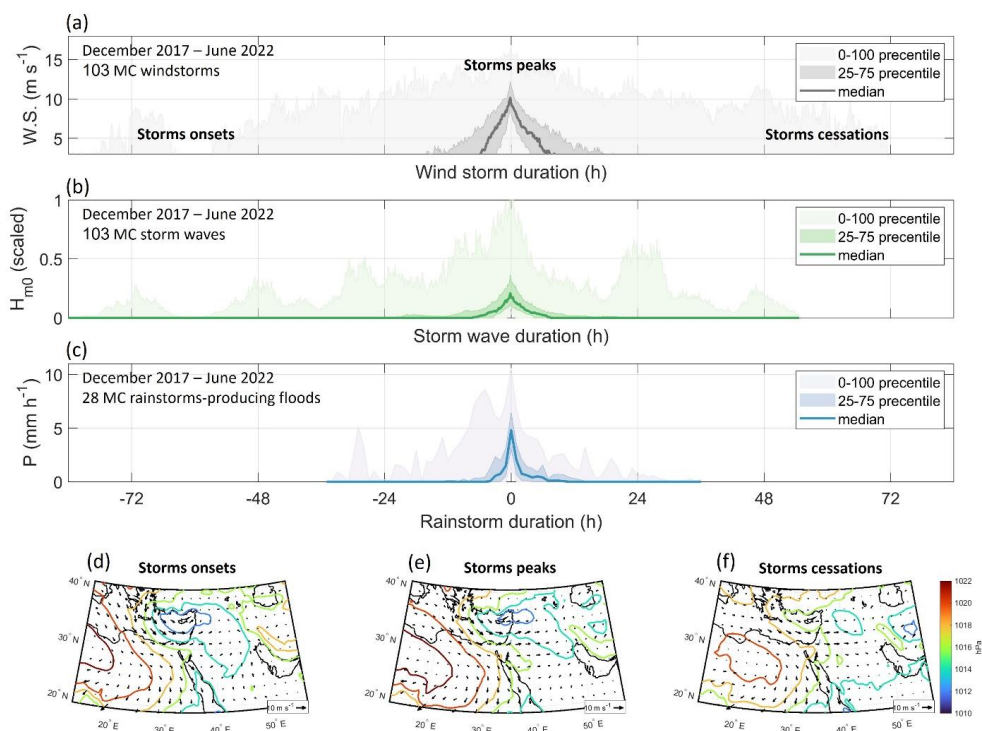
509 The rest of the flood-producing rainstorms (~15%) are attributed to ARSTs (Fig. 12b). These storms produced
510 low floods during the beginning and end of the hydrological season. This observation emphasizes the control of
511 MCs on geomorphic processes and delivery of sediments to the basin in this region (Fig. 12). For ARSTs, both
512 rainstorm duration and floods occurrence are uncorrelated with rainfall amounts (Fig. 12b); these complex
513 relations are attributed to the short duration and relatively high-intensity, localized rainfall associated with ARSTs
514 that a single rain gauge (Ma'ale Adumim, location in Fig. 2b) cannot capture, biasing the flood-producing rain
515 depth (e.g., Sharon, 1972; Marra and Morin, 2018).



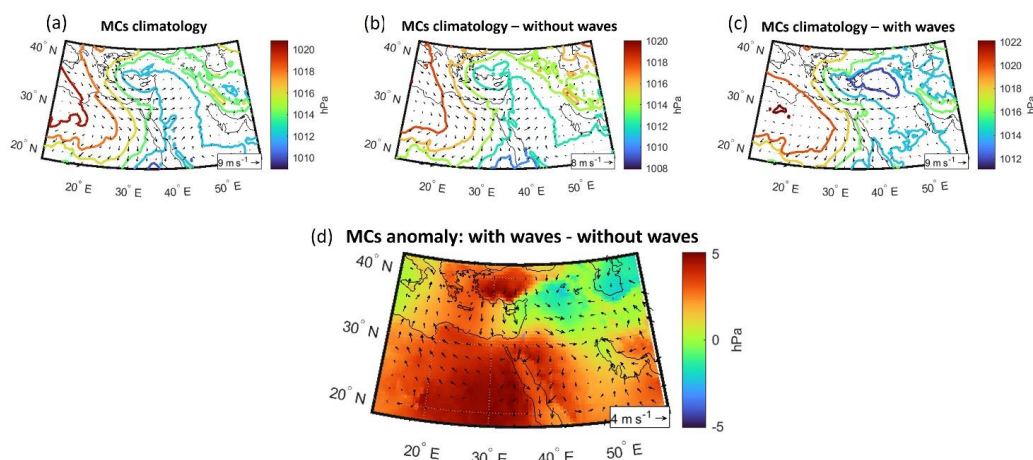
516 **Figure 11: The interaction between fluvial and coastal conveyors during five consecutive hydrological years 2017-2022.**
 517 **Hourly rain depth measured in Ma'ale Adumim (location in Fig. 2b) with classified flood-producing rainstorms (left**
 518 **axis; blue and orange bars, respectively). Vertical blue lines represent the occurrence of floods (Table S1). Waves with**
 519 **classified storm waves (reversed, right-axis; blue and yellow dots, respectively).**



520 **Figure 12: (a) Duration of wind versus wave storms (circles), the energy of a storm wave (circle size), and atmospheric**
 521 **CPs (MC-blue, RST-orange, PT-purple, SL-green). Storm wave energy was calculated for each storm according to**
 522 **$E \sim \sum H_{m0}^2$, and then scaled between 0 to 1 according to the full range of storm wave energies. (b) Rainfall depth versus**
 523 **rainstorm duration at rainstorms-producing floods (circles), the categories of floods (circle sizes), and CPs according**
 524 **to the same color coding as in (a).**



525 **Figure 13: The ‘mean’ (a) wind speed, (b) wave height, and (c) flood-producing rainstorms under MCs. Median storms**
 526 **values (solid lines), intermediate quantiles of the storms (25-75%) and the full range of values (0-100%) is indicated**
 527 **(shaded-colored areas). Composite mean pressure maps at the (d) onset, (e) peak, and (f) cessation of the wind-wave**
 528 **storms showing the mean synoptic-scale evolution/ climatology during the storms.**



529 **Figure 14: The climatology and anomaly of MCs producing and non-producing wind-wave storms. MCs climatology**
530 **composite pressure maps of (a) all days classified as MC (following Alpert et al., 2004), (b) the non-generating wind-**
531 **wave storms, (c) the generating wind-wave storms. (d) The difference (subtraction) between the generating and non-**
532 **generating MCs.**

533 5. Hydroclimatic signature in modern to paleo-sedimentary records

534 Following the detailed observations of waves, floods, and related sediment transport under MCs (Sect. 4), we
535 discuss here the accumulation and architecture of modern and paleo-Dead Sea coastal landforms formed over
536 longer time scales of decades to millennia. In Sect. 5.1, we discuss the accumulation of the Nahal Og modern-
537 recent environment evolving across the Dead Sea shelf and slope under rapid lake-level fall of the past decades.
538 Then, in Sect. 5.2, we present observations of a nearby stream and its coastal landforms accumulated on top of
539 the shelf during the last modern Dead Sea highstand. Finally, in Sect. 5.3, we extend the discussion to gain insights
540 into the architecture of fan deltas and paleo-beach berms formed during the Late Pleistocene at the foot of the
541 Dead Sea western escarpment.

542 5.1 The evolution of Modern lowstand coastal berms (Nahal Og)

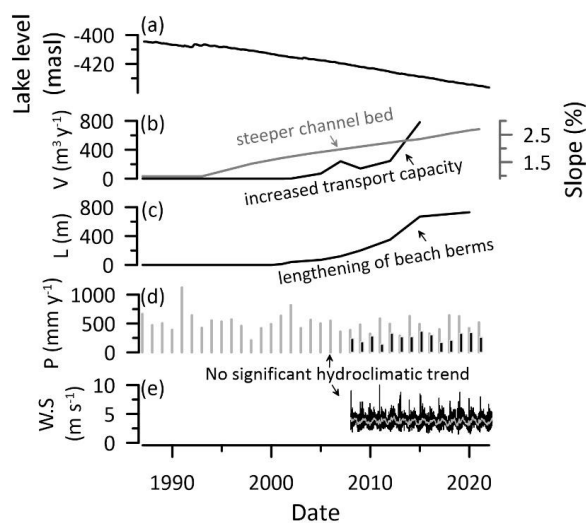
543 The sedimentary record of coarse-clastic beach berms at the Nahal Og mouth has accumulated since the early
544 2000s (Eyal et al., 2019) (Fig. 2d), pointing to three clear sedimentary/architectural trends over time: (i) Northward
545 deposition of beach berms that (ii) lengthen with time under waves action, and (iii) increased sediment volume
546 delivered by the incising and steepening stream to the receding shoreline (Fig. 15). The northward orientation of
547 deposition is attributed to MCs-generated winter storms and northward propagating waves. However, the latter
548 two trends contrast the hydroclimatic forcing of winter rain-floods and wind-waves that do not exhibit a significant
549 trend in the past decades (Sect. S2). If anything, there may be a regional drying trend due to the poleward shift of
550 the storm track and a decrease in total storm rainfall (e.g., Shohami et al., 2011; Zittis et al., 2022; Zappa et al.,
551 2015; Hochman et al., 2018; Armon et al., 2022).

552 Therefore, the intensified sediment delivery to the basin is attributed to the geometric response of the channel to
553 lake-level fall. Following the exposure of the Dead Sea shelf and steeper channel mouth gradients (~10%), a rapid



554 incision across the shelf was triggered (Eyal et al., 2019). An expanding knickzone evolved with higher gradients
555 migrating upstream (Ben Moshe et al., 2008), concurrently with channel deepening and narrowing that should
556 increase fluid shear stress exerted on the channel bed and bedload sediment flux to the channel mouth (Meyer-
557 Peter and Müller, 1948). Indeed, the transport rate across the shelf for a specific clast size increased over time
558 from tens to hundreds of meters per year over ~15 years (see discussion regarding the 'virtual velocity' in Eyal et
559 al., 2019). In larger spatio-temporal scales, it was shown that channel gradient is a first-order control on sediment
560 supply to river mouths together with the contributing drainage area (Syvitski and Milliman, 2007). The latter
561 factor is dominant along the global ocean shores during glacial periods when global sea level falls and watersheds
562 may merge over the exposed continental shelf (Mulder and Syvitski, 1996; BURGESS and HOVIUS, 1998),
563 supplying larger volumes of sediment into a certain lowstand delta (e.g., Anderson et al., 2016, for the rivers
564 draining into the Gulf of Mexico). The contribution of climate change during glacial lowstands is considered a
565 second order influencer (Syvitski and Milliman, 2007), with complex relations that may result in either increase
566 or decrease of the sediment delivery to channel mouths (e.g., Blum and Hattier-Womack, 2009) mainly of the
567 suspended sediment fraction (e.g., Mulder and Syvitski, 1996; Fagherazzi et al., 2004).

568 The lengthening of beach berms with time under annually similar wave climate is a less clear phenomenon as it
569 was concluded before that a single clast of a certain mass would travel a fixed, predictable distance under a given
570 distribution of wave heights within a storm (Eyal et al., 2021). This raises the question: why would larger sediment
571 volumes travel farther along the shore under a similar wave climate? Three mechanisms may explain this
572 observation: (i) The decay of wave orbital velocities with water depth (e.g., Dean and Dalrymple, 1991) results in
573 higher near-surface orbital velocities encountering large, thicker sediment volumes. Thus, the potential of gravels
574 to travel longer distances along the shore is higher for larger sediment volume. (ii) The probability of a clast to be
575 washed out of the swash zone during a storm coevally to the dominating stormy longshore transport (e.g., Benelli
576 et al., 2012). Lighter/smaller clasts have a higher probability to be washed out of the swash zone than
577 heavier/larger clasts that tend to travel down the beach slope under the influence of gravity (e.g., Grottoli et al.,
578 2015). Consequently, smaller sediment volumes, characterized by smaller grain-size distributions (Eyal et al.,
579 2019), have a higher probability to completely be washed out of the swash zone at early stages of the season,
580 forming shorter-extending beach berms. (iii) Reworking of beach berms between successive years. Lake-level
581 declines at $\sim 1.2 \text{ m y}^{-1}$ over the relatively steep ($\sim 10\%$) beach slope, exposing annually 10-15-m wide strip of the
582 previous year coastal sediment, leaving $<50\%$ of the coarse sediment submerged underwater. This way, sediments
583 that have travelled along the shore in the previous year, start moving from an 'advanced' location, and reach
584 farther northward distances. This inter-annual process is superimposed on the existing signal of increasing
585 sediment volumes conveyed to the coast with time. Gravels weighing several kilograms travel distances of
586 hundreds of meters during single storms between 2018-2022 (Figs. 5f, 9f), an order of magnitude longer distance
587 than the shortest beach berm preserved in the Nahal Og from the early 2000s with a length of tens of meters (Fig.
588 2d). This observation strengthens the assertion that for larger volumes of sediment, gravels are displaced farther
589 along the shore, and the inter-annual recycling between beach berms, may be superimposed on the signal of beach
590 berms lengthening with time.



604 **Figure 15: Reorganization and the buildup of lowstand sedimentary record under hydroclimatic forcing.** (a) Dead Sea
605 lake level. (b) Average channel slope of Nahal Og, measured between Highway 90 to the Dead Sea (Fig. 2c), increase
606 with time in response to rapid level decline (right axis; grey), the estimated increase in annual volume (V) of sediment
607 delivered to the channel mouth following Eyal et al., (2019) (left axis; black). (c) Increase in the length (L) of beach berms
608 with time. (d) Annual rainfall (P) in Ma'ale Adumim (black bars, 2008-2022) and Jerusalem (grey bars, 1985-
609 2022). (e) Wind speed (W.S) in Beit Ha'Arava (black line; daily mean, grey line; monthly mean, 2008-2022).

610

611 5.2 Modern highstand coastal landforms of a nearby stream (Nahal Qumeran)

612 The northward elongation of beach berms deposited during the highstand phase of the early 20th century Dead Sea
613 at the mouth of a nearby ephemeral stream, Nahal Qumeran (Fig. 16a-c) provides a wider perspective of our
614 analysis. The Nahal Qumeran catchment neighbors Nahal Og from the south (Fig. 2b,c), it has a smaller (47 km²)
615 and drier mean annual rain volume over its watershed of $8 \times 10^6 \text{ m}^3 \text{ y}^{-1}$ (Ben Moshe et al., 2008) than Nahal Og.
616 Between 1945 to 1960 the Dead Sea level was relatively stable, ranging between -390 to -395 mbsl, and Nahal
617 Qumeran was fluviially connected to the Dead Sea shores through a braided coarse-clastic fan-delta. During the
618 1960s and 1970s, with the onset of human-induced lake-level decline, the stream could keep pace with the slowly
619 regressive shoreline to feed its highstand fan-delta (Fig. 16b,c). During this interval, a series of beach berms
620 similar to those formed in Nahal Og, were formed, showing extension to the north from the Qumeran channel
621 mouth, fitting the above detected preferred directionality of winter winds and storm waves (Sect. 4). We do not
622 identify any trends of increased sediment volumes or lengthening of beach berms in the channel mouth as its base
623 level is approximately stable and the channel profile and sediment flux are not interrupted. Since the early 1970s
624 lake-level decline has accelerated, the channel did not keep pace with the rapid receding shoreline and low-
625 gradient mudflats emerged (see also Eyal et al., 2019; Enzel et al., 2022). At that moment, Nahal Qumeran stopped
626 responding to the rapid lake-level decline and became disconnected from the lake, showing no incision across the
627 shelf or any sediment delivery to the lake (Eyal et al., 2019). Instead, this stream maintains the buildup of an
628 alluvial fan prograding onto the mudflat platform, with no substantial impacts of the lake coastal hydrodynamics



629 that generate the northward depositional asymmetry, related to the regional forcing of MCs. It seems that as long
630 as the fluvial and coastal conveyors interact, regional hydroclimatology was manifested in northward elongating
631 beach berms, similar to Nahal Og. However, disconnecting the fluvial from the coastal conveyors, transforms the
632 channel mouth from a fan-delta into an alluvial fan that develops onto the mudflats regardless of the water body
633 hydrodynamics.

634

635 **5.3 Pleistocene Lake Lisan - sedimentary record of Nahal Tmarim**

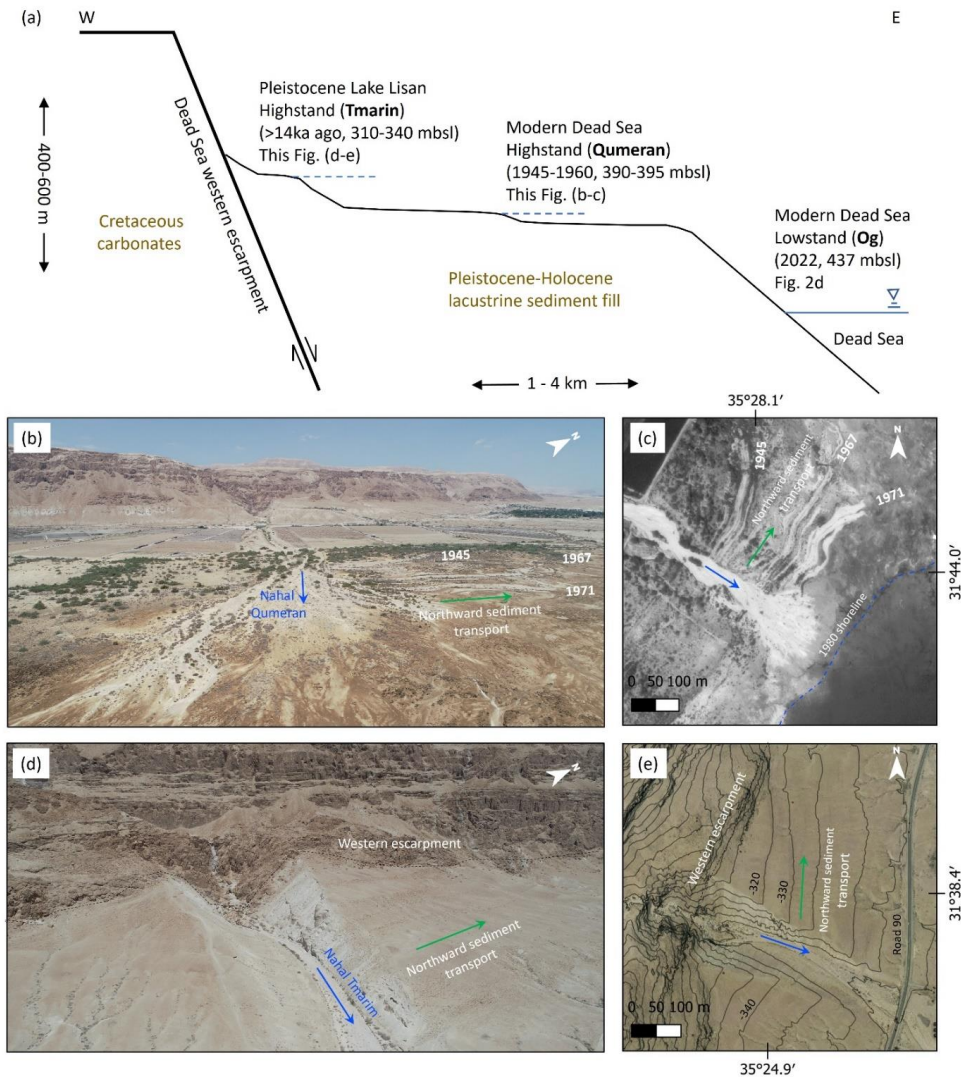
636 Following the observations from the modern Dead Sea in Nahal Og and Nahal Qumeran, we explore whether the
637 control of southern winds along the Dead Sea rift valley, had affected past deltaic-coastal sedimentary
638 morphology. At the foot of the western Dead Sea escarpment at stream outlets, Gilbert-type fan-deltas, alluvial
639 fans, and paleo-shorelines associated with the higher levels and recession of the Late Pleistocene Lake Lisan are
640 well-preserved (Fig. 16a,d,e; see Fig 2b for the extent of Lake Lisan) (e.g., Manspeizer, 1985; Frostick and Reid,
641 1989; Bowman, 1971, 2019). We have recognized an asymmetry in the deposition of fan-deltas along most of the
642 northwestern shores of the Dead Sea in both large and small streams; they present preferential deposition and
643 more pronounced shorelines north of the feeding canyon mouths (Sect. S7). Channel outlets from the Deas Sea
644 escarpment/cliff maintain their locations since the Late Pleistocene as successions of Lake Lisan deposits are
645 preserved inside deeply incised canyons at stream banks (e.g., Bartov et al., 2007). Thus, the depositional
646 geometry and asymmetry of the channel deposits are evaluated with respect to the channel outlet from the Dead
647 Sea escarpment as an indicator of their deposition due to funneled wind and wave storm direction in the Late
648 Pleistocene. Here we present an example from the outlet of Nahal Tmarim (~22 km² drainage area), located ~15
649 km south of Nahal Og (Fig. 2b,c). Its Pleistocene fan-delta and its recessional paleo-shorelines/beach berms are
650 deposited at elevations ranging between 310 to 330 mbsl, corresponding to lake level decline of the Late
651 Pleistocene to Holocene (e.g., Bartov et al., 2007). The depositional configuration shows the abovementioned
652 asymmetry, with most of the sediment volume of the fan-delta extends northward of the stream outlet from the
653 cliff (Fig. 16d,e); the surface area of deposits north of the channel outlet is four times larger than the depositional
654 area south of the outlet. Furthermore, sorting of cobbles-boulders is observed along the paleo-shorelines; clast
655 sizes decrease northward and away from the Tmarim channel outlet, whereas, practically, no shorelines/berms are
656 recognized south of the stream outlet. The fan-delta of current Nahal Tmarim is different from the modern fan-
657 deltas of Nahal Og and Nahal Qumeran in several aspects: (i) It is a thick (20-30 m) deposit with Gilbert-type
658 forests and paleo-shorelines preserved on its surface. (ii) There is some contribution of coarse materials to the
659 coastal system either directly through the cliff taluses or by debris flows occurring under exceptionally heavy
660 storms (David-Novak et al., 2004; Ahlborn et al., 2018). (iii) It was built during Lake Lisan highstand and got its
661 final geomorphic shape during the regression of the lake (27-14 ka ago) and the transition into the Holocene
662 conditions, 14-12 ka ago (e.g., Bowman, 2019). Despite these dissimilarities, the framework under which this
663 sedimentary record had evolved with the northward extension of the delta, is similar. It indicates a dominating
664 southern wind-wave regime and a signature on past sedimentary records during the latest Pleistocene, were very
665 similar to today.

666 The highest stand of Lake Lisan ca. 26,000 years ago reached 145-165 mbsl (Bowman and Gross, 1992; Bartov
667 et al., 2002; Abu Ghazleh and Kempe, 2009), and extended over 240 km, from the Sea of Galilee to the northern
668 Arava (e.g., Bartov 2007) (Fig. 2a). The potential length of the fetch at what is currently the northern Dead Sea



669 basin more than doubled from both the north and the south. Thus, both northerlies, presently driven by meso-scale
670 circulation of Mediterranean Sea breeze (e.g., Lensky et al., 2018), and southerlies, mainly driven by synoptic-
671 scale MCs, could have potentially generated waves high enough to transport gravels along the shores of the lake
672 in both directions. However, the observed preferential deposition asymmetry points to the southerlies control and
673 in turn, to MCs that generated these southerlies-driven-waves with transport of coarse gravels northward; there is
674 no evidence for a preferred fetch from the north.

675 Moreover, the northward directional organization of coarse sediments in the basin agrees with the increased
676 frequency of MCs during wetter intervals of high lake stands in the Dead Sea basin (Armon et al., 2019; Enzel et
677 al., 2008; Ben Dor et al., 2018). This inference is based on present-day climatology showing that wetter winters
678 and high-lake levels are characterized by higher frequencies of deeper and southerly displaced storm tracks of
679 MCs (e.g., Ben Dor et al., 2018; Enzel et al., 2008, 2003; Saaroni et al., 2010). Prevalence of more frequent,
680 deeper MCs during the wetter Late Pleistocene, should have been resulted in an intensified activation of the *fluvial*
681 and *coastal sediment conveyors*, compared with modern conditions, as MC is the only CP that can generate both
682 rainstorms and windstorms in this region. Floods were more intense and probably more frequent, they have
683 delivered amplified sediment fluxes into the basin (Bartov et al., 2007). Westerlies/southwesterlies funneled in
684 the rift valley into southerlies were more frequent and intensified, blowing over a longer lake fetch of
685 diluted/fresher and less dense water, thus generating higher waves, with maximum heights that exceeded the
686 modern 4 m. Such waves are characterized by higher fluid orbital velocities that generate higher forces to transport
687 larger boulders for longer distances along the coast.



688 Figure 16: Modern and paleo-northward-extending beach berms and fan deltas. (a) Schematic cross section from the
 689 western Dead Sea escarpment to the modern Dead Sea showing the stratigraphic/geomorphic location of the three
 690 geomorphic records discussed in the paper. For location of the sites see Fig. 2b-c. (b) Angular drone photograph of
 691 Nahal Qumeran, and (c) orthophoto of Nahal Qumeran (1980), both showing the northward extending beach berms
 692 deposited as long as the stream fed the earlier 20th century shorelines with sediments. Since lake level decline has
 693 accelerated, the stream did not keep pace with the receding shore and an alluvial fan begun developing on top of the
 694 exposed shelf. (d) Angular drone photograph of Nahal Tmarim, and (e) orthophoto of Nahal Tmarim (2012), both
 695 showing the norward deposition of fan-delta and beach berms under late Pleistocene Lake Lisan wind-wave regime.
 696 The asymmetry of sediment deposition to the north is evident also by looking at the elevation contours in (e), converging
 697 with steps of pleo-shorelines, with respect to the escarpment strike; northward of the channel, contours are sub-parallel
 698 to the escarpment direction, whereas they diagonally approach it on the southern part.



699 **6. Summary and conclusions**

700 Mediterranean cyclones are the main synoptic-scale generators of both rain and storm waves over the Dead Sea
701 region. Thus, they are also the main drivers for the coarse-clastic fluvial sediment flux into the lake and the
702 transport and sorting of clasts along shores. First, these MCs generate the high-magnitude synoptic wind with
703 westerly cyclonic circulation propagating to the northeastern Mediterranean. Near the surface and perpendicular
704 to this synoptic wind direction, the flow is funneled orographically along the Dead Sea rift valley into southerlies
705 that generate waves activating the *coastal conveyor*. Then, when the cyclone position migrates closer to the eastern
706 Mediterranean shoreline or is centered inland in Syria, the northern component of the wind becomes more
707 prominent, the southerly wave-producing winds decay, and rainfall evolves in the watershed over the Judean
708 Desert. The rainfall generates floods, which activate the *fluvial conveyor* within a few hours. Thus, fluvial
709 sediments reach the basin either coevally with or completely after the decay of the storm waves. Accordingly, the
710 longshore transport and sorting often occurs during the next storm in the same season, or infrequently, over the
711 same cyclonic system.

712 MCs-producing waves are, on average, ~ 10 hPa deeper, generating southern winds of up to 20 m s^{-1} that last >10
713 hours. When the wind-driven waves are higher than 0.6 m, the threshold for transport of a 1-kg clast, the coastal
714 conveyor is activated. When rainfall of >10 mm per storm accumulates at the center of the watershed, moderate
715 flood or larger are likely to activate the fluvial conveyor.

716 Although both the stream and coast are usually activated under MCs, the transport under storm waves is >5 -
717 times more frequent than the delivery of sediments by moderate or larger floods. This is geomorphologically
718 noticeable in the wave-dominated fan-delta, transformed into regressive beach berms extending northward of the
719 Nahal Og mouth. As the flood hydroclimatology shows no clear trend in recent decades, the increase of sediment
720 volume delivered to the channel mouth during this interval, is attributed to the response of the stream profile to
721 base level fall, the exposed stream mouth is steep and result in incising, steepening, and in increased bedload
722 transport capacity. Concurrently, under rather constant wave climate, this increase in sediment discharge is
723 associated with longer transportation distances of coarse gravels along the shore, and the increase of the beach
724 berms length with time.

725 Guided by the observation from modern environments, we recognized that similar directionality of the
726 hydroclimatology resulted in sedimentary deposition northward of canyon mouths in fan-deltas and coastal
727 deposits from the Late Pleistocene. This implies that over past millennia, MCs have played major role in
728 connecting fluvial delivery of coarse sediments, and their distribution in the lake and along its coasts.

729 **7. Data availability**

730 The data related to this work is available on Mendeley Data repository
731 <https://data.mendeley.com/drafts/65bhpwftrh> (Eyal et al., 2022), and in Table S1 in the supplement. Rain gauge
732 data were provided and pre-processed by the Israel Meteorological Service (<https://ims.data.gov.il/>; they are freely
733 available in Hebrew only). ERA5 data can be downloaded from <https://cds.climate.copernicus.eu> (Hersbach et al.,
734 2020). Flood reports from the years 2019-2022 were obtained from the Desert Floods Research Center
735 (<https://floods.org.il/english/>; they are freely available in Hebrew only).



736 **8. Video supplement**

737 The videos related to this article are available on <https://photos.app.goo.gl/rLysYEfoVSzyGdQo7>.

738 **9. Supplement link**

739 **10. Author contribution**

740 HE, MA, and NGL conceptualized this work. The methodology was developed by HE, MA, and NGL. Data
741 curation and formal analyses were performed by HE and MA. Funding was acquired by NGL, YE, and HE. NGL
742 and YE supervised the work. HE wrote the original draft of this paper, which was reviewed and edited by all
743 authors.

744 **11. Competing interests**

745 The authors declare that they have no conflict of interest.

746 **12. Acknowledgements**

747 This study was funded by the following grants: PI-NGL: ISF-1471/18, BSF-2018/035, NSF-BSF-2019/637; PI-
748 YE: ISF-946/18. HE is grateful to the Azrieli Foundation for the Azrieli Fellowship. MA was supported by an
749 ETH Zürich Postdoctoral Fellowship (Project No. 21-1 FEL-67), by the Stiftung für naturwissenschaftliche und
750 technische Forschung and the ETH Zürich Foundation. We thank Vladimir Lyakhovsky, Eckart Meiburg, Efrat
751 Morin and Itai Haviv for discussions and insights. We acknowledge Ziv Mor, Ido Sirota, Raanan Bodzin, Uri
752 Malik and Hallel Lutzky for the assistance in the field and laboratory and Liran Ben Moshe for the drone
753 photography. Dorita Rostkier-edelstein and Lida Shendrik are acknowledged for providing the updated synoptic
754 classifications following Alpert et al., 2004, and Yoav Levi for sharing the large IMS datasets of rain and wind.



755 **13. References**

- 756 Abu Ghazleh, S. and Kempe, S.: Geomorphology of Lake Lisan terraces along the eastern coast of the
757 Dead Sea, Jordan, *Geomorphology*, 108, 246–263, <https://doi.org/10.1016/j.geomorph.2009.02.015>, 2009.
- 758 Ahlborn, M., Armon, M., Ben Dor, Y., Neugebauer, I., Schwab, M. J., Tjallingii, R., Shoqeir, J. H.,
759 Morin, E., Enzel, Y., and Brauer, A.: Increased frequency of torrential rainstorms during a regional late
760 Holocene eastern Mediterranean drought, *Quat. Res.*, 89, 425–431, <https://doi.org/10.1017/qua.2018.9>, 2018.
- 761 Alpert, P. and Shay-El, Y.: The moisture source for the winter cyclones in the EM, *Isr. Meteorol. Res.*
762 *Pap.*, 5, 20–27, 1994.
- 763 Alpert, P. and Ziv, B.: The Sharav Cyclone: Observations and some theoretical considerations, *J.*
764 *Geophys. Res.*, 94, 18495, <https://doi.org/10.1029/JD094iD15p18495>, 1989.
- 765 Alpert, P., Neeman, B. U., and Shay-El, Y.: Climatological analysis of Mediterranean cyclones using
766 ECMWF data, *Tellus A Dyn. Meteorol. Oceanogr.*, 42, 65–77, <https://doi.org/10.3402/tellusa.v42i1.11860>,
767 1990a.
- 768 Alpert, P., Abramsky, R., and Neeman, B. U.: The prevailing summer synoptic system in Israel—
769 subtropical high, not Persian trough, *Isr. J. Earth Sci.*, 39, 93–102, 1990b.
- 770 Alpert, P., Shafir, H., and Issahary, D.: Recent changes in the climate at the Dead Sea—a preliminary
771 study, *Clim. Change*, 37, 513–537, <https://doi.org/https://doi.org/10.1023/A:1005330908974>, 1997.
- 772 Alpert, P., Osetinsky, I., Ziv, B., and Shafir, H.: A new seasons definition based on classified daily
773 synoptic systems: an example for the eastern Mediterranean, *Int. J. Climatol.*, 24, 1013–1021,
774 <https://doi.org/10.1002/joc.1037>, 2004a.
- 775 Alpert, P., Osetinsky, I., Ziv, B., and Shafir, H.: Semi-objective classification for daily synoptic
776 systems: application to the eastern Mediterranean climate change, *Int. J. Climatol.*, 24, 1001–1011,
777 <https://doi.org/10.1002/joc.1036>, 2004b.
- 778 Amit, R. and Gerson, R.: The evolution of holocene reg (gravelly) soils in deserts: An example from
779 the dead sea region, *CATENA*, 13, 59–79, [https://doi.org/10.1016/S0341-8162\(86\)80005-4](https://doi.org/10.1016/S0341-8162(86)80005-4), 1986.
- 780 Anderson, J. B., Wallace, D. J., Simms, A. R., Rodriguez, A. B., Weight, R. W. R., and Taha, Z. P.:
781 Recycling sediments between source and sink during a eustatic cycle: Systems of late Quaternary northwestern
782 Gulf of Mexico Basin, *Earth-Science Rev.*, 153, 111–138, <https://doi.org/10.1016/j.earscirev.2015.10.014>, 2016.
- 783 Arbel, S., Getker, M., Arazi, A., Yosi, B., Moshe, G., Efraim, F., and Alon, M.: Data of rain and floods
784 of exceptional events in the hydrological year 2006-2007, special report M-84, 2009.
- 785 Armon, M., Dente, E., Smith, J. A., Enzel, Y., and Morin, E.: Synoptic-Scale Control over Modern
786 Rainfall and Flood Patterns in the Levant Drylands with Implications for Past Climates, *J. Hydrometeorol.*, 19,
787 1077–1096, <https://doi.org/10.1175/JHM-D-18-0013.1>, 2018.
- 788 Armon, M., Morin, E., and Enzel, Y.: Overview of modern atmospheric patterns controlling rainfall
789 and floods into the Dead Sea: Implications for the lake’s sedimentology and paleohydrology, *Quat. Sci. Rev.*,
790 216, 58–73, <https://doi.org/10.1016/j.quascirev.2019.06.005>, 2019.
- 791 Armon, M., Marra, F., Enzel, Y., Rostkier-Edelstein, D., and Morin, E.: Radar-based characterisation
792 of heavy precipitation in the eastern Mediterranean and its representation in a convection-permitting model,
793 *Hydrol. Earth Syst. Sci.*, 24, 1227–1249, <https://doi.org/10.5194/hess-24-1227-2020>, 2020.
- 794 Armon, M., Marra, F., Enzel, Y., Rostkier-Edelstein, D., Garfinkel, C. I., Adam, O., Dayan, U., and



- 795 Morin, E.: Reduced Rainfall in Future Heavy Precipitation Events Related to Contracted Rain Area Despite
796 Increased Rain Rate, *Earth's Futur.*, 10, e2021EF002397, <https://doi.org/10.1029/2021EF002397>, 2022.
- 797 Ashton, A. D. and Giosan, L.: Wave-angle control of delta evolution, *Geophys. Res. Lett.*, 38, n/a-n/a,
798 <https://doi.org/10.1029/2011GL047630>, 2011.
- 799 Ashton, A. D., Hutton, E. W. H., Kettner, A. J., Xing, F., Kallumadikal, J., Nienhuis, J., and Giosan,
800 L.: Progress in coupling models of coastline and fluvial dynamics, *Comput. Geosci.*, 53, 21–29,
801 <https://doi.org/10.1016/j.cageo.2012.04.004>, 2013.
- 802 Bárdossy, A. and Filiz, F.: Identification of flood producing atmospheric circulation patterns, *J.*
803 *Hydrol.*, 313, 48–57, <https://doi.org/10.1016/j.jhydrol.2005.02.006>, 2005.
- 804 Bartov, Y., Stein, M., Enzel, Y., Agnon, A., and Reches, Z.: Lake Levels and Sequence Stratigraphy of
805 Lake Lisan, the Late Pleistocene Precursor of the Dead Sea, *Quat. Res.*, 57, 9–21,
806 <https://doi.org/10.1006/qres.2001.2284>, 2002.
- 807 Bartov, Y., Goldstein, S. L., Stein, M., and Enzel, Y.: Catastrophic arid episodes in the Eastern
808 Mediterranean linked with the North Atlantic Heinrich events, *Geology*, 31, 439, [https://doi.org/10.1130/0091-7613\(2003\)031<0439:CAEITE>2.0.CO;2](https://doi.org/10.1130/0091-7613(2003)031<0439:CAEITE>2.0.CO;2), 2003.
- 810 Bartov, Y., Bookman, R., and Enzel, Y.: Current depositional environments at the Dead Sea margins as
811 indicators of past lake levels, in: *New Frontiers in Dead Sea Paleoenvironmental Research*, vol. 401, Geological
812 Society of America, 127–140, [https://doi.org/10.1130/2006.2401\(08\)](https://doi.org/10.1130/2006.2401(08)), 2006.
- 813 Bartov, Y., Enzel, Y., Porat, N., and Stein, M.: Evolution of the Late Pleistocene Holocene Dead Sea
814 Basin from Sequence Stratigraphy of Fan Deltas and Lake-Level Reconstruction, *J. Sediment. Res.*, 77, 680–692,
815 <https://doi.org/10.2110/jsr.2007.070>, 2007.
- 816 Belachsen, I., Marra, F., Peleg, N., and Morin, E.: Convective rainfall in a dry climate: relations with
817 synoptic systems and flash-flood generation in the Dead Sea region, *Hydrol. Earth Syst. Sci.*, 21, 5165–5180,
818 <https://doi.org/10.5194/hess-21-5165-2017>, 2017.
- 819 Benelli, G., Pozzebon, A., Bertoni, D., and Sarti, G.: An RFID-Based Toolbox for the Study of Under-
820 and Outside-Water Movement of Pebbles on Coarse-Grained Beaches, *IEEE J. Sel. Top. Appl. Earth Obs.*
821 *Remote Sens.*, 5, 1474–1482, <https://doi.org/10.1109/JSTARS.2012.2196499>, 2012.
- 822 Bitan, A.: The wind regime in the north-west section of the Dead-Sea, *Arch. für Meteorol. Geophys.*
823 *und Bioklimatologie Ser. B*, 22, 313–335, <https://doi.org/10.1007/BF02246585>, 1974.
- 824 Bitan, A.: The influence of the special shape of the dead-sea and its environment on the local wind
825 system, *Arch. für Meteorol. Geophys. und Bioklimatologie Ser. B*, 24, 283–301,
826 <https://doi.org/10.1007/BF02263460>, 1976.
- 827 Blum, M. D., Martin, J., Milliken, K., and Garvin, M.: Paleovalley systems: Insights from Quaternary
828 analogs and experiments, *Earth-Science Rev.*, 116, 128–169, <https://doi.org/10.1016/j.earscirev.2012.09.003>,
829 2013.
- 830 BLUM, M. D. and HATTIER-WOMACK, J.: Climate Change, Sea-Level Change, and Fluvial
831 Sediment Supply to Deepwater Depositional Systems, in: *External Controls of Deep-Water Depositional*
832 *Systems*, SEPM (Society for Sedimentary Geology), 15–39, <https://doi.org/10.2110/sepm.092.015>, 2009.
- 833 Bookman, R., Bartov, Y., Enzel, Y., and Stein, M.: Quaternary lake levels in the Dead Sea basin: two
834 centuries of research, *Geol. Soc. Am. Spacial Pap.*, 401, 155–170, [https://doi.org/10.1130/2006.2401\(10\).For](https://doi.org/10.1130/2006.2401(10).For),



- 835 2006.
- 836 Borga, M., Comiti, F., Ruin, I., and Marra, F.: Forensic analysis of flash flood response, *WIREs Water*,
- 837 6, e1338, <https://doi.org/10.1002/wat2.1338>, 2019.
- 838 Bowman, D.: Geomorphology of the shore terraces of the late pleistocene Lisan lake (Israel),
- 839 *Palaeogeogr. Palaeoclimatol. Palaeoecol.*, 9, 183–209, [https://doi.org/10.1016/0031-0182\(71\)90031-9](https://doi.org/10.1016/0031-0182(71)90031-9), 1971.
- 840 Bowman, D.: The Regional Approach: Alluvial Fans along the Dead Sea-Arava Rift Valley, in:
- 841 *Principles of Alluvial Fan Morphology*, Springer Netherlands, Dordrecht, 135–151, [https://doi.org/10.1007/978-](https://doi.org/10.1007/978-94-024-1558-2_19)
- 842 [94-024-1558-2_19](https://doi.org/10.1007/978-94-024-1558-2_19), 2019.
- 843 Bowman, D. and Gross, T.: The highest stand of Lake Lisan: ~ 150 meter below MSL, *Isr. J. Earth-*
- 844 *Sciences*, 41, 233–237, 1992.
- 845 Bowman, D., Banet-Davidovich, D., Bruins, H. J., and Plicht, J. Van der: Dead Sea shoreline facies
- 846 with seismically-induced soft-sediment deformation structures, Israel, *Isr. J. Earth Sci.*, 49, 197–214,
- 847 <https://doi.org/10.1560/GXHT-AK5W-46EF-VTR8>, 2000.
- 848 Bowman, D., Svoray, T., Devora, S., Shapira, I., and Laronne, J. B.: Geomorphology Extreme rates of
- 849 channel incision and shape evolution in response to a continuous , rapid base-level fall , the Dead Sea , Israel,
- 850 *Geomorphology*, 114, 227–237, <https://doi.org/10.1016/j.geomorph.2009.07.004>, 2010.
- 851 Bridge, J. S.: The interaction between channel geometry, water flow, sediment transport and deposition
- 852 in braided rivers, *Geol. Soc. London, Spec. Publ.*, 75, 13–71, <https://doi.org/10.1144/GSL.SP.1993.075.01.02>,
- 853 1993.
- 854 BURGESS, P. M. and HOVIUS, N.: Rates of delta progradation during highstands: consequences for
- 855 timing of deposition in deep-marine systems, *J. Geol. Soc. London.*, 155, 217–222,
- 856 <https://doi.org/10.1144/gsjgs.155.2.0217>, 1998.
- 857 Coleman, J. M. and Prior, D. B.: Deltaic environments of deposition, in: *M 31: Sandstone Depositional*
- 858 *Environments*, AAPG Special Volumes, 139–178, 1982.
- 859 David-Novak, H. Ben, Morin, E., and Enzel, Y.: Modern extreme storms and the rainfall thresholds for
- 860 initiating debris flows on the hyperarid western escarpment of the Dead Sea, Israel, *Geol. Soc. Am. Bull.*, 116,
- 861 718, <https://doi.org/10.1130/B25403.2>, 2004.
- 862 Dayan, U. and Morin, E.: Flash flood–producing rainstorms over the Dead Sea: A review, in: *New*
- 863 *Frontiers in Dead Sea Paleoenvironmental Research*, vol. 401, Geological Society of America, 53–62,
- 864 [https://doi.org/10.1130/2006.2401\(04\)](https://doi.org/10.1130/2006.2401(04)), 2006.
- 865 Dayan, U., Ricaud, P., Zbinden, R., and Dulac, F.: Atmospheric pollution over the eastern
- 866 Mediterranean during summer – a review, *Atmos. Chem. Phys.*, 17, 13233–13263, [https://doi.org/10.5194/acp-](https://doi.org/10.5194/acp-17-13233-2017)
- 867 [17-13233-2017](https://doi.org/10.5194/acp-17-13233-2017), 2017.
- 868 Dayan, U., Lensky, I. M., Ziv, B., and Khain, P.: Atmospheric conditions leading to an exceptional
- 869 fatal flash flood in the Negev Desert, Israel, *Nat. Hazards Earth Syst. Sci.*, 21, 1583–1597,
- 870 <https://doi.org/10.5194/nhess-21-1583-2021>, 2021.
- 871 Dean, R. G. and Dalrymple, R. A.: *Water Wave Mechanics for Engineers and Scientists*, WORLD
- 872 *SCIENTIFIC*, <https://doi.org/10.1142/1232>, 1991.
- 873 Dente, E., Lensky, N. G., Morin, E., Grodek, T., Sheffer, N. A., and Enzel, Y.: Geomorphic Response
- 874 of a Low-Gradient Channel to Modern, Progressive Base-Level Lowering: Nahal HaArava, the Dead Sea, *J.*



- 875 Geophys. Res. Earth Surf., 122, 2468–2487, <https://doi.org/10.1002/2016JF004081>, 2017.
- 876 Dente, E., Lensky, N. G., Morin, E., Dunne, T., and Enzel, Y.: Sinuosity evolution along an incising
877 channel: New insights from the Jordan River response to the Dead Sea level fall, Earth Surf. Process.
878 Landforms, <https://doi.org/10.1002/esp.4530>, 2018.
- 879 Dente, E., Lensky, N. G., Morin, E., and Enzel, Y.: From straight to deeply incised meandering
880 channels: Slope impact on sinuosity of confined streams, Earth Surf. Process. Landforms, 46, 1041–1054,
881 <https://doi.org/10.1002/esp.5085>, 2021.
- 882 Ben Dor, Y., Armon, M., Ahlborn, M., Morin, E., Erel, Y., Brauer, A., Schwab, M. J., Tjallingii, R.,
883 and Enzel, Y.: Changing flood frequencies under opposing late Pleistocene eastern Mediterranean climates, Sci.
884 Rep., 8, 8445, <https://doi.org/10.1038/s41598-018-25969-6>, 2018.
- 885 Elliot, T.: Deltas, edited by: Reading, H., Oxford, 113–154 pp., 1986.
- 886 Enzel, Y. and Bar-Yosef, O.: Quaternary of the Levant, edited by: Enzel, Y. and Bar-Yosef, O.,
887 Cambridge University Press, <https://doi.org/10.1017/9781316106754>, 2017.
- 888 Enzel, Y., Bookman, R., Sharon, D., Gvirtzman, H., Dayan, U., Ziv, B., and Stein, M.: Late Holocene
889 climates of the Near East deduced from Dead Sea level variations and modern regional winter rainfall, Quat.
890 Res., 60, 263–273, <https://doi.org/10.1016/j.yqres.2003.07.011>, 2003.
- 891 Enzel, Y., Agnon, A., and Stein, M.: New Frontiers in Dead Sea Paleoenvironmental Research,
892 Geological Society of America, <https://doi.org/10.1130/SPE401>, 2006.
- 893 Enzel, Y., Amit, R., Dayan, U., Crouvi, O., Kahana, R., Ziv, B., and Sharon, D.: The climatic and
894 physiographic controls of the eastern Mediterranean over the late Pleistocene climates in the southern Levant
895 and its neighboring deserts, Glob. Planet. Change, 60, 165–192,
896 <https://doi.org/10.1016/j.gloplacha.2007.02.003>, 2008.
- 897 Enzel, Y., Mushkin, A., Groisman, M., Calvo, R., Eyal, H., and Lensky, N.: The modern wave-induced
898 coastal staircase morphology along the western shores of the Dead Sea, Geomorphology, 408, 108237,
899 <https://doi.org/10.1016/j.geomorph.2022.108237>, 2022.
- 900 Eyal, H., Dente, E., Haviv, I., Enzel, Y., Dunne, T., and Lensky, N. G.: Fluvial incision and coarse
901 gravel redistribution across the modern Dead Sea shelf as a result of base-level fall, Earth Surf. Process.
902 Landforms, 44, 2170–2185, <https://doi.org/10.1002/esp.4640>, 2019.
- 903 Eyal, H., Enzel, Y., Meiburg, E., Vowinkel, B., and Lensky, N. G.: How Does Coastal Gravel Get
904 Sorted Under Stormy Longshore Transport?, Geophys. Res. Lett., 48, e2021GL095082,
905 <https://doi.org/10.1029/2021GL095082>, 2021.
- 906 Eyal, H., Armon, M., Enzel, Y., and Lensky, N. G.: Synoptic- to meso-scale circulation connects
907 fluvial and coastal gravel conveyors and directional deposition of coastal landforms in the Dead Sea basin,
908 Mendeley Data, V1, <https://doi.org/10.17632/65bhpwfrh.1>, 2022.
- 909 Fagherazzi, S.: Modeling fluvial erosion and deposition on continental shelves during sea level cycles,
910 J. Geophys. Res., 109, F03010, <https://doi.org/10.1029/2003JF000091>, 2004.
- 911 FROSTICK, L. E. and REID, I. A. N.: Climatic versus tectonic controls of fan sequences: lessons from
912 the Dead Sea, Israel, J. Geol. Soc. London., 146, 527–538, <https://doi.org/10.1144/gsjgs.146.3.0527>, 1989.
- 913 Galloway, W. E.: Process framework for describing the morphologic and stratigraphic evolution of
914 deltaic depositional systems, 87–98, 1975.



- 915 Garfunkel, Z. and Ben-Avraham, Z.: The structure of the Dead Sea basin, *Tectonophysics*, 266, 155–
916 176, [https://doi.org/10.1016/S0040-1951\(96\)00188-6](https://doi.org/10.1016/S0040-1951(96)00188-6), 1996.
- 917 Gertman, I. and Hecht, A.: The Dead Sea hydrography from 1992 to 2000, *J. Mar. Syst.*, 35, 169–181,
918 [https://doi.org/10.1016/S0924-7963\(02\)00079-9](https://doi.org/10.1016/S0924-7963(02)00079-9), 2002.
- 919 Goldreich, Y.: The spatial distribution of annual rainfall in Israel ? a review, *Theor. Appl. Climatol.*,
920 50, 45–59, <https://doi.org/10.1007/BF00864902>, 1994.
- 921 Goldreich, Y.: *The Climate of Israel*, Springer US, Boston, MA, <https://doi.org/10.1007/978-1-4615-0697-3>, 2003.
- 923 Goldreich, Y., Mozes, H., and Rosenfeld, D.: Radar analysis of cloud systems and their rainfall yield in
924 Israel, *Isr. J. Earth Sci.*, 53, 63–76, 2004.
- 925 Goodwin, I. D., Mortlock, T. R., and Browning, S.: Tropical and extratropical-origin storm wave types
926 and their influence on the East Australian longshore sand transport system under a changing climate, *J.*
927 *Geophys. Res. Ocean.*, 121, 4833–4853, <https://doi.org/10.1002/2016JC011769>, 2016.
- 928 Graf, M., Sprenger, M., Lohmann, U., Seibt, C., and Hofmann, H.: Evaluating the suitability of the
929 SWAN/COSMO-2 model system to simulate short-crested surface waves for a narrow lake with complex
930 bathymetry, *Meteorol. Zeitschrift*, 22, 257–272, <https://doi.org/10.1127/0941-2948/2013/0442>, 2013.
- 931 Grosse, G., Schirrmeyer, L., Kunitsky, V. V., and Hubberten, H.: The use of CORONA images in
932 remote sensing of periglacial geomorphology: an illustration from the NE Siberian coast, *Permafrost*.
933 *Process.*, 16, 163–172, <https://doi.org/10.1002/ppp.509>, 2005.
- 934 Grottole, E., Bertoni, D., Ciavola, P., and Pozzebon, A.: Short term displacements of marked pebbles in
935 the swash zone: Focus on particle shape and size, *Mar. Geol.*, 367, 143–158,
936 <https://doi.org/10.1016/j.margeo.2015.06.006>, 2015.
- 937 Hamdani, I., Assouline, S., Tanny, J., Lensky, I. M., Gertman, I., Mor, Z., and Lensky, N. G.: Seasonal
938 and diurnal evaporation from a deep hypersaline lake: The Dead Sea as a case study, *J. Hydrol.*, 562, 155–167,
939 <https://doi.org/10.1016/j.jhydrol.2018.04.057>, 2018.
- 940 Hansford, M. R. and Plink-Björklund, P.: River discharge variability as the link between climate and
941 fluvial fan formation, *Geology*, 48, 952–956, <https://doi.org/10.1130/G47471.1>, 2020.
- 942 Haviv, I.: *Mechanics, morphology and evolution of vertical knickpoints (waterfalls) along the bedrock*
943 *channels of the Dead Sea western tectonic escarpment*, The Hebrew University of Jerusalem, 2007.
- 944 Hersbach, H., Bell, B., Berrisford, P., Hirahara, S., Horányi, A., Muñoz-Sabater, J., Nicolas, J., Peubey,
945 C., Radu, R., Schepers, D., Simmons, A., Soci, C., Abdalla, S., Abellan, X., Balsamo, G., Bechtold, P., Biavati,
946 G., Bidlot, J., Bonavita, M., Chiara, G., Dahlgren, P., Dee, D., Diamantakis, M., Dragani, R., Flemming, J.,
947 Forbes, R., Fuentes, M., Geer, A., Haimberger, L., Healy, S., Hogan, R. J., Hólm, E., Janisková, M., Keeley, S.,
948 Laloyaux, P., Lopez, P., Lupu, C., Radnoti, G., Rosnay, P., Rozum, I., Vamborg, F., Villaume, S., and Thépaut,
949 J.: The ERA5 global reanalysis, *Q. J. R. Meteorol. Soc.*, 146, 1999–2049, <https://doi.org/10.1002/qj.3803>, 2020.
- 950 Van Hijum, E. and Pilarczyk, K. W.: *Gravel beaches: equilibrium profile and longshore transport of*
951 *coarse material under regular and irregular wave attack*, Hydraulics laboratory, 1982.
- 952 Hochman, A., Mercogliano, P., Alpert, P., Saaroni, H., and Bucchignani, E.: High-resolution projection
953 of climate change and extremity over Israel using COSMO-CLM, *Int. J. Climatol.*, 38, 5095–5106,
954 <https://doi.org/10.1002/joc.5714>, 2018.



- 955 Huntington, E.: Palestine and its Transformation, Houghton Mifflin, 1911.
- 956 Kahana, R., Ziv, B., Enzel, Y., and Dayan, U.: Synoptic climatology of major floods in the Negev
957 Desert, Israel, *Int. J. Climatol.*, 22, 867–882, <https://doi.org/10.1002/joc.766>, 2002.
- 958 Karimpour, A. and Chen, Q.: Wind wave analysis in depth limited water using OCEANLYZ, A
959 MATLAB toolbox, *Comput. Geosci.*, 106, 181–189, <https://doi.org/10.1016/j.cageo.2017.06.010>, 2017.
- 960 Kiro, Y., Goldstein, S. L., Garcia-Veigas, J., Levy, E., Kushnir, Y., Stein, M., and Lazar, B.:
961 Relationships between lake-level changes and water and salt budgets in the Dead Sea during extreme aridities in
962 the Eastern Mediterranean, *Earth Planet. Sci. Lett.*, 464, 211–226, <https://doi.org/10.1016/j.epsl.2017.01.043>,
963 2017.
- 964 Kunin, P., Alpert, P., and Rostkier-Edelstein, D.: Investigation of sea-breeze/foehn in the Dead Sea
965 valley employing high resolution WRF and observations, *Atmos. Res.*, 229, 240–254,
966 <https://doi.org/10.1016/j.atmosres.2019.06.012>, 2019.
- 967 Kushnir, Y., Dayan, U., Ziv, B., Morin, E., and Enzel, Y.: Climate of the Levant, in: Quaternary of the
968 Levant, Cambridge University Press, 31–44, <https://doi.org/10.1017/9781316106754.004>, 2017.
- 969 Lekach, J. and Enzel, Y.: Flood-duration-integrated stream power and frequency magnitude of >50-
970 year-long sediment discharge out of a hyperarid watershed, *Earth Surf. Process. Landforms*, 46, 1348–1362,
971 <https://doi.org/10.1002/esp.5104>, 2021.
- 972 Lensky, I. M. and Dayan, U.: Continuous detection and characterization of the Sea Breeze in clear sky
973 conditions using Meteosat Second Generation, *Atmos. Chem. Phys.*, 12, 6505–6513,
974 <https://doi.org/10.5194/acp-12-6505-2012>, 2012.
- 975 Lensky, I. M. and Dayan, U.: Satellite observations of land surface temperature patterns induced by
976 synoptic circulation, *Int. J. Climatol.*, 35, 189–195, <https://doi.org/10.1002/joc.3971>, 2015.
- 977 Lensky, N. G., Dvorkin, Y., Lyakhovskiy, V., Gertman, I., and Gavrieli, I.: Water, salt, and energy
978 balances of the Dead Sea, *Water Resour. Res.*, 41, 1–13, <https://doi.org/10.1029/2005WR004084>, 2005.
- 979 Lensky, N. G., Lensky, I. M., Peretz, A., Gertman, I., Tanny, J., and Assouline, S.: Diurnal Course of
980 Evaporation From the Dead Sea in Summer: A Distinct Double Peak Induced by Solar Radiation and Night Sea
981 Breeze, *Water Resour. Res.*, 54, 150–160, <https://doi.org/10.1002/2017WR021536>, 2018.
- 982 Longuet-Higgins, M. S.: Longshore currents generated by obliquely incident sea waves: 1, *J. Geophys.*
983 *Res.*, 75, 6778–6789, 1970.
- 984 Manspeizer, W.: The Dead Sea Rift: Impact of climate and tectonism on Pleistocene and Holocene
985 sedimentation, 1985.
- 986 Marra, F. and Morin, E.: Autocorrelation structure of convective rainfall in semiarid-arid climate
987 derived from high-resolution X-Band radar estimates, *Atmos. Res.*, 200, 126–138,
988 <https://doi.org/10.1016/j.atmosres.2017.09.020>, 2018.
- 989 Marra, F., Borga, M., and Morin, E.: A Unified Framework for Extreme Subdaily Precipitation
990 Frequency Analyses Based on Ordinary Events, *Geophys. Res. Lett.*, 47, e2020GL090209,
991 <https://doi.org/10.1029/2020GL090209>, 2020.
- 992 Marra, F., Armon, M., Adam, O., Zoccatelli, D., Gazal, O., Garfinkel, C. I., Rostkier-Edelstein, D.,
993 Dayan, U., Enzel, Y., and Morin, E.: Toward Narrowing Uncertainty in Future Projections of Local Extreme
994 Precipitation, *Geophys. Res. Lett.*, 48, e2020GL091823, <https://doi.org/10.1029/2020GL091823>, 2021.



- 995 Marra, F., Armon, M., and Morin, E.: Coastal and orographic effects on extreme precipitation revealed
996 by weather radar observations, *Hydrol. Earth Syst. Sci.*, 26, 1439–1458, [https://doi.org/10.5194/hess-26-1439-](https://doi.org/10.5194/hess-26-1439-2022)
997 2022, 2022.
- 998 Meadows, G. A., Meadows, L. A., Wood, W. L., Hubertz, J. M., and Perlin, M.: The Relationship
999 between Great Lakes Water Levels, Wave Energies, and Shoreline Damage, *Bull. Am. Meteorol. Soc.*, 78, 675–
1000 682, [https://doi.org/10.1175/1520-0477\(1997\)078<0675:TRBGLW>2.0.CO;2](https://doi.org/10.1175/1520-0477(1997)078<0675:TRBGLW>2.0.CO;2), 1997.
- 1001 Merz, B., Blöschl, G., Vorogushyn, S., Dottori, F., Aerts, J. C. J. H., Bates, P., Bertola, M., Kemter,
1002 M., Kreibich, H., Lall, U., and Macdonald, E.: Causes, impacts and patterns of disastrous river floods, *Nat. Rev.*
1003 *Earth Environ.*, 2, 592–609, <https://doi.org/10.1038/s43017-021-00195-3>, 2021.
- 1004 Meyer-Peter, E. and Müller, R.: Formulas for bed-load transport, in: IAHSR 2nd meeting, Stockholm,
1005 appendix 2, 1948.
- 1006 Molina, R., Manno, G., Lo Re, C., Anfuso, G., and Ciraolo, G.: Storm Energy Flux Characterization
1007 along the Mediterranean Coast of Andalusia (Spain), *Water*, 11, 509, <https://doi.org/10.3390/w11030509>, 2019.
- 1008 Montgomery, D. R. and Buffington, J. M.: Channel-reach morphology in mountain drainage basins,
1009 *Bull. Geol. Soc. Am.*, 109, 596–611, [https://doi.org/10.1130/0016-7606\(1997\)109<0596:CRMIMD>2.3.CO;2](https://doi.org/10.1130/0016-7606(1997)109<0596:CRMIMD>2.3.CO;2),
1010 1997.
- 1011 Morin, E., Jacoby, Y., Navon, S., and Bet-Halachmi, E.: Towards flash-flood prediction in the dry
1012 Dead Sea region utilizing radar rainfall information, *Adv. Water Resour.*, 32, 1066–1076,
1013 <https://doi.org/10.1016/j.advwatres.2008.11.011>, 2009.
- 1014 Ben Moshe, L., Haviv, I., Enzel, Y., Zilberman, E., and Matmon, A.: Incision of alluvial channels in
1015 response to a continuous base level fall: Field characterization, modeling, and validation along the Dead Sea,
1016 *Geomorphology*, 93, 524–536, <https://doi.org/10.1016/j.geomorph.2007.03.014>, 2008.
- 1017 Mulder, T. and Syvitski, J. P. M.: Climatic and Morphologic Relationships of Rivers: Implications of
1018 Sea-Level Fluctuations on River Loads, *J. Geol.*, 104, 509–523, <https://doi.org/10.1086/629849>, 1996.
- 1019 Naor, R., Potchter, O., Shafir, H., and Alpert, P.: An observational study of the summer Mediterranean
1020 Sea breeze front penetration into the complex topography of the Jordan Rift Valley, *Theor. Appl. Climatol.*, 127,
1021 275–284, <https://doi.org/10.1007/s00704-015-1635-3>, 2017.
- 1022 Neev, D. and Emery, K. O.: The Dead Sea: depositional processes and environments of evaporites,
1023 1967.
- 1024 Neugebauer, I., Schwab, M. J., Waldmann, N. D., Tjallingii, R., Frank, U., Hadzhiivanova, E.,
1025 Naumann, R., Taha, N., Agnon, A., Enzel, Y., and Brauer, A.: Hydroclimatic variability in the Levant during the
1026 early last glacial (~117–75 ka) derived from micro-facies analyses of deep Dead Sea sediments, *Clim. Past*, 12,
1027 75–90, <https://doi.org/10.5194/cp-12-75-2016>, 2016.
- 1028 Palchan, D., Neugebauer, I., Amitai, Y., Waldmann, N. D., Schwab, M. J., Dulski, P., Brauer, A.,
1029 Stein, M., Erel, Y., and Enzel, Y.: North Atlantic controlled depositional cycles in MIS 5e layered sediments
1030 from the deep Dead Sea basin, *Quat. Res.*, 87, 168–179, <https://doi.org/10.1017/qua.2016.10>, 2017.
- 1031 Postma, G.: An analysis of the variation in delta architecture, *Terra Nov.*, 2, 124–130,
1032 <https://doi.org/10.1111/j.1365-3121.1990.tb00052.x>, 1990.
- 1033 Postma, G.: Sea-level-related architectural trends in coarse-grained delta complexes, *Sediment. Geol.*,
1034 98, 3–12, [https://doi.org/10.1016/0037-0738\(95\)00024-3](https://doi.org/10.1016/0037-0738(95)00024-3), 1995.



- 1035 Pringle, J. and Stretch, D. D.: On a new statistical wave generator based on atmospheric circulation
1036 patterns and its applications to coastal shoreline evolution, *Comput. Geosci.*, 149, 104707,
1037 <https://doi.org/10.1016/j.cageo.2021.104707>, 2021.
- 1038 Pringle, J., Stretch, D. D., and Bárdossy, A.: Automated classification of the atmospheric circulation
1039 patterns that drive regional wave climates, *Nat. Hazards Earth Syst. Sci.*, 14, 2145–2155,
1040 <https://doi.org/10.5194/nhess-14-2145-2014>, 2014.
- 1041 Pringle, J., Stretch, D. D., and Bárdossy, A.: On linking atmospheric circulation patterns to extreme
1042 wave events for coastal vulnerability assessments, *Nat. Hazards*, 79, 45–59, [https://doi.org/10.1007/s11069-015-](https://doi.org/10.1007/s11069-015-1825-4)
1043 1825-4, 2015.
- 1044 Reid, I., Frostick, L. E., and Layman, J. T.: The incidence and nature of bedload transport during flood
1045 flows in coarse-grained alluvial channels, *Earth Surf. Process. Landforms*, 10, 33–44,
1046 <https://doi.org/10.1002/esp.3290100107>, 1985.
- 1047 Rinat, Y., Marra, F., Armon, M., Metzger, A., Levi, Y., Khain, P., Vadislavsky, E., Rosensaft, M., and
1048 Morin, E.: Hydrometeorological analysis and forecasting of a 3 d flash-flood-triggering desert rainstorm, *Nat.*
1049 *Hazards Earth Syst. Sci.*, 21, 917–939, <https://doi.org/10.5194/nhess-21-917-2021>, 2021.
- 1050 Rodwell, M. J. and Hoskins, B. J.: Monsoons and the dynamics of deserts, *Q. J. R. Meteorol. Soc.*, 122,
1051 1385–1404, <https://doi.org/10.1002/qj.49712253408>, 1996.
- 1052 Saaroni, H., Ziv, B., Bitan, A., and Alpert, P.: Easterly Wind Storms over Israel, *Theor. Appl.*
1053 *Climatol.*, 59, 61–77, <https://doi.org/10.1007/s007040050013>, 1998.
- 1054 Saaroni, H., Halfon, N., Ziv, B., Alpert, P., and Kutiel, H.: Links between the rainfall regime in Israel
1055 and location and intensity of Cyprus lows, *Int. J. Climatol.*, 30, 1014–1025, <https://doi.org/10.1002/joc.1912>,
1056 2010.
- 1057 Segal, M., Mahrer, Y., and Pielke, R. A.: A study of meteorological patterns associated with a lake
1058 confined by mountains—the Dead Sea case, *Q. J. R. Meteorol. Soc.*, 109, 549–564, 1983.
- 1059 Sharon, D.: The spottiness of rainfall in a desert area, *J. Hydrol.*, 17, 161–175,
1060 [https://doi.org/10.1016/0022-1694\(72\)90002-9](https://doi.org/10.1016/0022-1694(72)90002-9), 1972.
- 1061 Sharon, D. and Kutiel, H.: The distribution of rainfall intensity in Israel, its regional and seasonal
1062 variations and its climatological evaluation, *J. Climatol.*, 6, 277–291, <https://doi.org/10.1002/joc.3370060304>,
1063 1986.
- 1064 Shentsis, I., Laronne, J. B., and Alpert, P.: Red Sea Trough flood events in the Negev, Israel (1964–
1065 2007), *Hydrol. Sci. J.*, 57, 42–51, <https://doi.org/10.1080/02626667.2011.636922>, 2012.
- 1066 Shohami, D., Dayan, U., and Morin, E.: Warming and drying of the eastern Mediterranean: Additional
1067 evidence from trend analysis, *J. Geophys. Res. Atmos.*, 116, n/a–n/a, <https://doi.org/10.1029/2011JD016004>,
1068 2011.
- 1069 Sirota, I., Enzel, Y., Mor, Z., Ben Moshe, L., Eyal, H., Lowenstein, T. K., and Lensky, N. G.:
1070 Sedimentology and stratigraphy of a modern halite sequence formed under Dead Sea level fall, *Sedimentology*,
1071 68, 1069–1090, <https://doi.org/10.1111/sed.12814>, 2021.
- 1072 Solari, S. and Alonso, R.: A New Methodology for Extreme Waves Analysis Based on Weather-
1073 Patterns Classification Methods, *Coast. Eng. Proc.*, 23, <https://doi.org/10.9753/icce.v35.waves.23>, 2017.
- 1074 Steirou, E., Gerlitz, L., Apel, H., and Merz, B.: Links between large-scale circulation patterns and



- 1075 streamflow in Central Europe: A review, *J. Hydrol.*, 549, 484–500, 2017.
- 1076 Syvitski, J. P. M. and Milliman, J. D.: Geology, Geography, and Humans Battle for Dominance over
1077 the Delivery of Fluvial Sediment to the Coastal Ocean, *J. Geol.*, 115, 1–19, <https://doi.org/10.1086/509246>,
1078 2007.
- 1079 Syvitski, J. P. M., Kettner, A. J., Overeem, I., Hutton, E. W. H., Hannon, M. T., Brakenridge, G. R.,
1080 Day, J., Vörösmarty, C., Saito, Y., Giosan, L., and Nicholls, R. J.: Sinking deltas due to human activities, *Nat.*
1081 *Geosci.*, 2, 681–686, <https://doi.org/10.1038/ngeo629>, 2009.
- 1082 Torfstein, A., Goldstein, S. L., Stein, M., and Enzel, Y.: Impacts of abrupt climate changes in the
1083 Levant from Last Glacial Dead Sea levels, *Quat. Sci. Rev.*, 69, 1–7,
1084 <https://doi.org/10.1016/j.quascirev.2013.02.015>, 2013.
- 1085 Torfstein, A., Goldstein, S. L., Kushnir, Y., Enzel, Y., Haug, G., and Stein, M.: Dead Sea drawdown
1086 and monsoonal impacts in the Levant during the last interglacial, *Earth Planet. Sci. Lett.*, 412, 235–244,
1087 <https://doi.org/10.1016/j.epsl.2014.12.013>, 2015.
- 1088 Tsvieli, Y. and Zangvil, A.: Synoptic climatological analysis of Red Sea Trough and non-Red Sea
1089 Trough rain situations over Israel, *Adv. Geosci.*, 12, 137–143, <https://doi.org/10.5194/adgeo-12-137-2007>,
1090 2007.
- 1091 Tyrllis, E. and Lelieveld, J.: Climatology and Dynamics of the Summer Etesian Winds over the Eastern
1092 Mediterranean*, *J. Atmos. Sci.*, 70, 3374–3396, <https://doi.org/10.1175/JAS-D-13-035.1>, 2013.
- 1093 de Vries, A. J., Tyrllis, E., Edry, D., Krichak, S. O., Steil, B., and Lelieveld, J.: Extreme precipitation
1094 events in the Middle East: Dynamics of the Active Red Sea Trough, *J. Geophys. Res. Atmos.*, 118, 7087–7108,
1095 <https://doi.org/10.1002/jgrd.50569>, 2013.
- 1096 Vüllers, J., Mayr, G. J., Corsmeier, U., and Kottmeier, C.: Characteristics and evolution of diurnal
1097 foehn events in the Dead Sea valley, *Atmos. Chem. Phys.*, 18, 18169–18186, [https://doi.org/10.5194/acp-18-](https://doi.org/10.5194/acp-18-18169-2018)
1098 18169-2018, 2018.
- 1099 Wang, C., Zheng, S., Wang, P., and Hou, J.: Interactions between vegetation, water flow and sediment
1100 transport: A review, *J. Hydrodyn.*, 27, 24–37, [https://doi.org/10.1016/S1001-6058\(15\)60453-X](https://doi.org/10.1016/S1001-6058(15)60453-X), 2015.
- 1101 WRIGHT, L. D.: Sediment transport and deposition at river mouths: A synthesis, *Geol. Soc. Am. Bull.*,
1102 88, 857, [https://doi.org/10.1130/0016-7606\(1977\)88<857:STADAR>2.0.CO;2](https://doi.org/10.1130/0016-7606(1977)88<857:STADAR>2.0.CO;2), 1977.
- 1103 Zak, I.: The geology of Mt. Sedom, Hebrew University, 1967.
- 1104 Zappa, G., Hoskins, B. J., and Shepherd, T. G.: The dependence of wintertime Mediterranean
1105 precipitation on the atmospheric circulation response to climate change, *Environ. Res. Lett.*, 10, 104012,
1106 <https://doi.org/10.1088/1748-9326/10/10/104012>, 2015.
- 1107 Zittis, G., Almazroui, M., Alpert, P., Ciais, P., Cramer, W., Dahdal, Y., Fnais, M., Francis, D.,
1108 Hadjinicolaou, P., Howari, F., Jrrar, A., Kaskaoutis, D. G., Kulmala, M., Lazoglou, G., Mihalopoulos, N., Lin,
1109 X., Rudich, Y., Sciare, J., Stenchikov, G., Xoplaki, E., and Lelieveld, J.: Climate Change and Weather Extremes
1110 in the Eastern Mediterranean and Middle East, *Rev. Geophys.*, 60, e2021RG000762,
1111 <https://doi.org/10.1029/2021RG000762>, 2022.
- 1112 Ziv, B., Saaroni, H., and Alpert, P.: The factors governing the summer regime of the eastern
1113 Mediterranean, *Int. J. Climatol.*, 24, 1859–1871, <https://doi.org/10.1002/joc.1113>, 2004.
- 1114 Ziv, B., Harpaz, T., Saaroni, H., and Blender, R.: A new methodology for identifying daughter



- 1115 cyclogenesis: application for the Mediterranean Basin, *Int. J. Climatol.*, 35, 3847–3861,
1116 <https://doi.org/10.1002/joc.4250>, 2015.
- 1117 Ziv, B., Saaroni, H., Etkin, A., Harpaz, T., and Shendrik, L.: Formation of cyclones over the East
1118 Mediterranean within Red-Sea Troughs, *Int. J. Climatol.*, 42, 577–596, <https://doi.org/10.1002/joc.7261>, 2022.
- 1119 Zoccatelli, D., Marra, F., Armon, M., Rinat, Y., Smith, J. A., and Morin, E.: Contrasting rainfall-runoff
1120 characteristics of floods in desert and Mediterranean basins, *Hydrol. Earth Syst. Sci.*, 23, 2665–2678,
1121 <https://doi.org/10.5194/hess-23-2665-2019>, 2019.
- 1122